

# Beam Plasma Interaction and Nonlinear Processes in Solar Wind Plasma

by

Md Manir Hossain

A thesis submitted in partial fulfillment of the requirements for the degree of

Master of Science

Department of Physics

University of Alberta

©Md Manir Hossain, 2018

## Abstract

Langmuir amplitude modulations and harmonic waves, generated by solar wind electron beams, are commonly observed in type III solar radio bursts. Various mechanisms have been proposed for the origin of these waves, but there is still ongoing debate on how the observation of continuous type III radiation over large distances, e.g., from Sun to Earth, can be reconciled with the picture of fast beam stabilization by plateau formation. In this context, the occurrence of current-driven Langmuir oscillations in plasmas with plateau distributions offers a relatively simple mechanism of electromagnetic emission. The saturation process of the beam instability is accompanied with the formation of a plateau distribution and the saturated state represents a current which drives homogeneous electric field oscillations at the plasma frequency. A plasma system composed of main and beam plasma electrons with finite temperature is considered and Ampere's law is used instead of Poisson's equation to describe the mechanism of current drive in plasmas. Results of using Poisson's equation and Ampere's law are compared by using particle-in-cell simulations. Possible modulational instabilities that generate solitary structure are investigated. Theoretical and simulation results are compared with space observations.

Dedicated to my loving wife Marzia Akter.

## Acknowledgements

All praises to Almighty Allah, the most benevolent and merciful and the Creator of the whole universe, who enabled me to complete this research work successfully.

I would like to express my sincere and hearty appreciation to my supervisor Dr. Richard Sydora for his constant encouragement, constructive guidance and helpful suggestions during the course of this research work. I deeply appreciate his energy, enthusiasm, and ability to see and formulate new and exciting physical problems.

I am very grateful to Dr. Konrad Sauer for his useful discussion on the electromagnetic plasma model and Soheli Bhuiyan for his discussion on MATLAB codes.

I would like to thank my family members for the support they have provided me throughout my life. I express my gratitude to my wife, Marzia Akter, whose love, encouragement and support helped me to successfully complete this thesis.

In conclusion, I would like to recognize that this research would not have been possible without the financial assistance of the University of Alberta's Faculty of Graduate Studies and Research and the Department of Physics, and express my thanks to those agencies.

# Contents

<b>Contents</b>	<b>v</b>
<b>List of Tables</b>	<b>viii</b>
<b>List of Figures</b>	<b>ix</b>
<b>1 Physics of the Solar Wind</b>	<b>1</b>
1.1 The Sun . . . . .	1
1.2 Solar Wind . . . . .	2
1.3 Solar Radio Bursts . . . . .	4
1.3.1 Type I . . . . .	6
1.3.2 Type II . . . . .	6
1.4 Type III Bursts . . . . .	6
1.4.1 Frequency Extent . . . . .	6
1.4.2 Burst Duration . . . . .	7
1.4.3 Frequency Drift Rate . . . . .	7
1.4.4 Source Flux . . . . .	8
1.4.5 Source Size . . . . .	8
1.4.6 Brightness . . . . .	8
1.4.7 Harmonic Structure . . . . .	8
1.5 Fundamentals of Plasmas . . . . .	9
1.5.1 Plasmas . . . . .	9
1.5.2 Debye Shielding and Debye Length . . . . .	10
1.5.3 Plasma Frequency . . . . .	11
1.5.4 Criteria for Plasma . . . . .	11

## CONTENTS

1.6	Plasma Waves . . . . .	12
1.6.1	Electron Plasma Waves . . . . .	13
1.6.2	Ion-Acoustic Waves . . . . .	13
1.6.3	Electromagnetic waves . . . . .	14
<b>2</b>	<b>Motivation and Approach</b>	<b>15</b>
2.1	Motivation . . . . .	15
2.2	Overview of Approach . . . . .	20
<b>3</b>	<b>Linear Analysis</b>	<b>22</b>
3.1	Introduction . . . . .	22
3.2	Electron Beams . . . . .	22
3.3	Plasma Wave Instability . . . . .	23
3.3.1	Instability in Plasma . . . . .	23
3.3.2	Instability in Cold Beam Plasma . . . . .	24
3.4	Water-bag Distribution . . . . .	24
3.5	Model Fluid Equations . . . . .	25
3.6	Derivation of the Dispersion Relation . . . . .	27
3.7	Dispersion Analysis . . . . .	29
3.8	Summary . . . . .	32
<b>4</b>	<b>Particle-in-Cell Model</b>	<b>34</b>
4.1	Introduction . . . . .	34
4.2	Overview of PIC model . . . . .	35
4.3	Electrostatic Plasma Simulation Model . . . . .	36
4.4	Electromagnetic Plasma Simulation Model . . . . .	38
4.5	Summary . . . . .	39
<b>5</b>	<b>Beam Plasma Instability Analysis</b>	<b>40</b>
5.1	Introduction . . . . .	40
5.2	Current Driven Langmuir Oscillations . . . . .	41
5.3	Modulational Instability: Electrostatic Case . . . . .	44
5.4	Modulational Instability: Electromagnetic Case . . . . .	51
5.5	Connection to the Space Observation . . . . .	58

## CONTENTS

5.6 Summary . . . . .	60
<b>6 Summary and Future Work</b>	<b>62</b>
<b>Bibliography</b>	<b>64</b>
<b>Appendix Dispersion Matrix Formulation</b>	<b>70</b>

# List of Tables

1.1	Typical parameters of the solar wind at 1 AU. . . . .	3
1.2	Comparison of typical fast and solar slow wind properties at 1 AU.	4
1.3	Types of Solar Radio Bursts . . . . .	5

# List of Figures

1.1	Streams of solar wind from the Sun [ <a href="http://nasa.gov/SolarWind">nasa.gov/SolarWind</a> ]. . . . .	2
1.2	Schematic radio dynamic spectrum showing different types of solar radio bursts [ <a href="#">4</a> ]. . . . .	5
1.3	Type III radio bursts are created by electrons and can be observed in space and/or at Earth [ <a href="#">6</a> ]. . . . .	7
2.1	Dynamic spectrum of a local type III radio burst (fast drifting emission from 5 MHz down to 30 kHz) and associated Langmuir waves (non-drifting emissions in the frequency interval 27-32 kHz [ <a href="#">34</a> ]). . . . .	16
2.2	Bump-on-tail distributions [ <a href="#">37</a> ]. . . . .	17
2.3	The spectrum observed during the type III event by the Time Domain Sampler [ <a href="#">34</a> ] . . . . .	18
2.4	Langmuir wave packet observed during the type III event by the Time Domain Sampler [ <a href="#">34</a> ]. . . . .	18
2.5	Positions of STEREO A and B for 23-Nov-2016 21:00 UT [ <a href="http://stereo-ssc.nascom.nasa.gov/where.shtml">stereo-ssc.nascom.nasa.gov/where.shtml</a> ]. . . . .	19
3.1	Distribution function versus velocity normalized to thermal speed shows the transition from (a) pronounced beam instability to (d) a stable state.[ <a href="#">55</a> ]. . . . .	25
3.2	Schematic of the electromagnetic beam plasma system. . . . .	26

## LIST OF FIGURES

3.3	Sketch of the transition from a) pronounced beam instability to c) a saturated stable state, where $\mu = n_{po}/n_{eo} = 0.01$ , $\theta = 30^\circ$ , $c/V_{Te}=0.05$ and parameters a) beam velocity $V_p = 12$ , and thermal velocity $U_p = 2$ . (b) $V_p = 10$ , $U_p = 3$ , and (c) $V_p = 9$ , $U_p = 4$ . . . . .	29
3.4	Sketch of the transition from a) pronounced beam instability to c) a saturated stable state, where $\mu = n_{po}/n_{eo} = 0.01$ , beam velocity $V_p = 12$ , thermal velocity $U_p = 1$ , $c/V_{Te}=0.05$ and a) $\theta = 30^\circ$ , (b) $\theta = 50^\circ$ , and (c) $\theta = 65^\circ$ . . . . .	29
3.5	Showing the change of wave modes and maximum growth rate of the beam instability with the change of main to beam electron density ratio, $\mu = n_{po}/n_{eo}$ where $\theta = 30^\circ$ , $c/V_{Te} = 0.05$ , $V_p = 10$ , $U_p = 3$ , and (a) $\mu = 0.01$ , (b) $\mu = 0.05$ , (c) $\mu = 0.09$ . . . . .	31
3.6	Showing the change of wave modes and maximum growth rate of the beam instability with the change of $c/V_{Te}$ where $\theta = 30^\circ$ , $\mu = 0.01$ , $V_p = 12$ , $U_p = 3$ , and (a) $c/V_{Te} = 0.01$ , (b) $c/V_{Te} = 0.03$ , (c) $c/V_{Te} = 0.05$ . . . . .	31
5.1	The $x-t$ evolution of the electric field, found from PIC simulation using Poisson equation, exhibits the typical stripe pattern of a propagating wave. . . . .	42
5.2	Result of PIC simulation using Poisson equation shows the temporal evolution of the electric field at $x/\lambda_D = 250$ . . . . .	42
5.3	The $x-t$ evolution of the electric field, found from PIC simulation using Ampere's Law, exhibits Langmuir oscillations. . . . .	43
5.4	Result of PIC simulation using Ampere's Law shows the temporal evolution of the electric field at $x/\lambda_D = 250$ . . . . .	43
5.5	Shows the space-time evolution of the electric field amplitude $E(x, t)/E_0$ where field structuring become visible and solitons are formed due to the modulational instability. . . . .	45
5.6	Shows spatial profile related to Fig. 5.5 at $\omega_e t = 800$ . . . . .	45
5.7	Shows temporal variation of of the electric field $E(t)/E_0$ at $x/\lambda_D = 220$ . . . . .	46

## LIST OF FIGURES

5.8	Shows the space-time evolution of the ion density $n_i(x, t)/n_0$ . Density structuring become visible and cavitons are formed due to the modulational instability. . . . .	47
5.9	Shows spatial profile related to Fig. 5.8 at $\omega_e t = 800$ . . . . .	47
5.10	Shows the power spectrum of the electric field $E(\omega)$ at $x/\lambda_D = 220$ . . . . .	48
5.11	Shows low frequency power spectrum of the electric field $E(\omega)$ at $x/\lambda_D = 220$ . . . . .	48
5.12	Shows how the value of the electric field $E(k)$ varies with different wave mode number in $k$ - space for different time ranges. . . . .	49
5.13	Shows the space-time evolution of $x$ - component of the electric field amplitude $E_x(x, t)/E_0$ for $\omega_e t = 0$ to $\omega_e t = 1000$ . . . . .	50
5.14	Shows the space-time evolution of $x$ - component of the electric field amplitude $E_x(x, t)/E_0$ for $\omega_e t = 1000$ to $\omega_e t = 3000$ . . . . .	50
5.15	Extended view of the space-time evolution of $x$ - component of the electric field amplitude $E_x(x, t)/E_0$ for $\omega_e t = 1850$ to $\omega_e t = 3000$ . . . . .	51
5.16	Shows spatial profile related to Figure 5.14 at $\omega_e t = 2400$ . . . . .	51
5.17	Shows temporal variation of $x$ - component of the electric field $E_x(t)$ at $x/\lambda_D = 166$ . . . . .	52
5.18	Shows power spectrum of $x$ - component of the electric field $E_x(\omega)$ for $x/\lambda_D = 166$ . . . . .	52
5.19	Shows the space-time evolution of $y$ - component of the electric field amplitude $E_y(x, t)/E_0$ . . . . .	53
5.20	Shows spatial profile related to Figure 5.19 at $\omega_e t = 2200$ . . . . .	53
5.21	Shows temporal variation of $y$ - component of the electric field $E_y(t)$ at $x/\lambda_D = 166$ . . . . .	54
5.22	Shows power spectrum of $y$ - component of the electric field $E_y(\omega)$ for $x/\lambda_D = 166$ . . . . .	54
5.23	Shows the space-time evolution of $z$ - component of the magnetic field amplitude $B_z(x, t)/B_0$ . . . . .	55
5.24	Shows spatial profile related to Figure 5.23 at $\omega_e t = 2200$ . . . . .	55
5.25	Shows the space-time evolution of the ion density $n_i(x, t)/n_0$ for electromagnetic case. . . . .	56
5.26	Shows spatial profile related to Figure 5.25 at $\omega_e t = 2400$ . . . . .	56

## LIST OF FIGURES

5.27	Shows temporal variation of the ion density $n_i(t)$ at $x/\lambda_D = 166$ .	57
5.28	Waveform and spectrum of Langmuir waves and density perturbations of the event observed by STEREO A on 19 December 2011 at 13:50:55.160 UT. (a) Waveform of electric field. (b) Density perturbations. (c) Power spectrum near plasma frequency. (d) Power spectrum at low frequency [67]. . . . .	59

# Chapter 1

## Physics of the Solar Wind

### 1.1 The Sun

The Sun is the heart of our solar system which holds 99.8 percent of the solar system's mass and is roughly 109 times the diameter of the Earth. Temperature in the core of the sun is about 15 million degrees Celsius while the temperature in the visible part is about 5500 degrees Celsius. The sun and its atmosphere have several zones and layers. The solar interior is made up of the core, the radiative zone, the Tachocline, and the convective zone. The visible surface of the Sun is the photosphere. This layer is about 480 kilometers thick and contains a gas of neutral atoms with a small fraction of it in the ionized form. Sun emits most of the visible light from this layer. Above the photosphere, there is a layer of 2000-3000 kilometers thick atmosphere called chromosphere. The Chromosphere is a quiet and non-magnetic layer of the solar atmosphere. It has a colorful appearance just before and after a total eclipse. Temperature at the bottom of the chromosphere is about 4300 Kelvin, so it is hotter than the photosphere. The Sun's hot outer atmosphere is called corona. The corona extends more than a solar radius above the solar surface. Beyond that is the solar wind, an outflow of gas from the corona. Sun is the main source of solar plasma. Plasmas are found in the solar atmosphere, the interplanetary medium, the planetary magnetospheres and the planetary ionosphere.

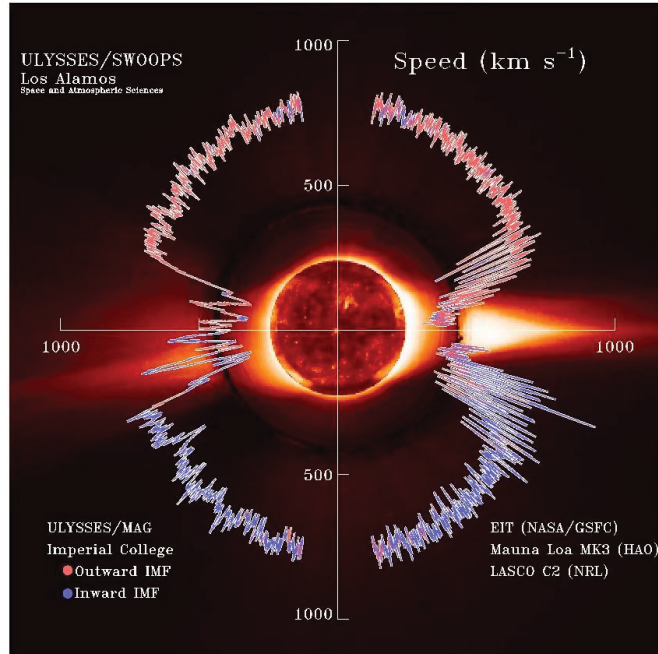


Figure 1.1: Streams of solar wind from the Sun [nasa.gov/SolarWind].

## 1.2 Solar Wind

Streams of energized charged particles (electrons, protons, alpha particles, etc.) are emitted radially outward from the sun at a speed of 500 km/s to 900 km/s. This outflow of plasma is the consequence of the supersonic expansion of the solar corona. Heating of the solar corona creates high temperatures and the plasma particles can escape the Sun's gravity into interplanetary space because of their high energy. This streaming and expanding plasma is known as solar wind. Density, temperature, and speed of the solar wind vary over time and longitude. The density of the solar wind decreases with the inverse square of the distance from the Sun and its temperature decreases adiabatically. Near the Earth, at 1 Astronomical Unit (AU), typical values of the solar wind parameters are summarized in Table 1.1. At the Earth's orbit, the solar wind is quite dilute and thus electrically highly conducting. The solar coronal magnetic field is 'frozen' into the streaming solar wind plasma and drawn outward by expanding solar wind flow, gradually becoming the interplanetary magnetic field of the order of  $\approx 5nT$  near Earth's orbit. Thus the solar wind plays an important role in shaping and stimulating

planetary magnetospheres [1].

Table 1.1: Typical parameters of the solar wind at 1 AU.

<b>Parameter</b>	<b>Electron</b>	<b>Ion</b>
Density ( $\rho$ ), $cm^{-3}$	8.7	8.7
Temperature (T), $eV$	12	10
Drift Velocity $v_d$ , $km/s$	468	468
Thermal velocity ( $V_t$ ), $km/s$	$2.05 \times 10^3$	438
Debye length ( $\lambda_d$ ), $m$	8.7	7.97
Plasma frequency ( $\omega_e$ ), $rad/s$	$1.66 \times 10^5$	$3.9 \times 10^3$
Gyrofrequency ( $\Omega_g$ ), $rad/s$	$1.8 \times 10^3$	0.96
Gyroradius ( $r$ ), $km$	1.1	489

There are two different kinds of solar wind namely fast solar wind and slow solar wind. The fast solar winds are originated from polar holes and its speed at 1 AU is about 250 to 400  $km/s$ . The slow solar winds are originated from equatorial belt having speed 400-800  $km/s$  at near Earth. Comparison of typical fast and slow wind properties near at 1 AU is given in Table 1.2 [2].

Table 1.2: Comparison of typical fast and solar slow wind properties at 1 AU.

<b>Parameter</b>	<b>Fast</b>	<b>Slow</b>
Source,	Coronal holes	Streamer belt
Flow Speed ( $v_p$ ), $km/s$	400-800	250-400
Electron Density ( $\rho_e$ ) $\times 10^6 m^{-3}$	2.5	7
Electron Temperature ( $T_e$ ) $\times 10^5 m^5$	1	1.3
Total energy flux density, $erg - cm^{-2}s^{-1}$	1.43	1.55
Ram pressure (P), $\times 10^6 Pa$	2.6	2.1

### 1.3 Solar Radio Bursts

Solar radio bursts are the first radio phenomena identified by radar scientists. They are classified by their frequency drift rate. By studying the rapidly varying component over a range of frequencies one can classify the emissions into five principal types [3] as follows

1. Noise-storm bursts (Type I)
2. Slow-drift bursts (Type II)
3. Fast-drift bursts (Type III)
4. Broad-band continuum emission (Type IV)
5. Continuum emission at meter wavelengths (Type V)

A schematic diagram of different types of solar radio bursts is shown in figure 1.2. Among these five different types of bursts, three of them (type I, type II and type III) are more important for the study of plasma emission. Classification of these three types of bursts is summarized the Table 1.3.

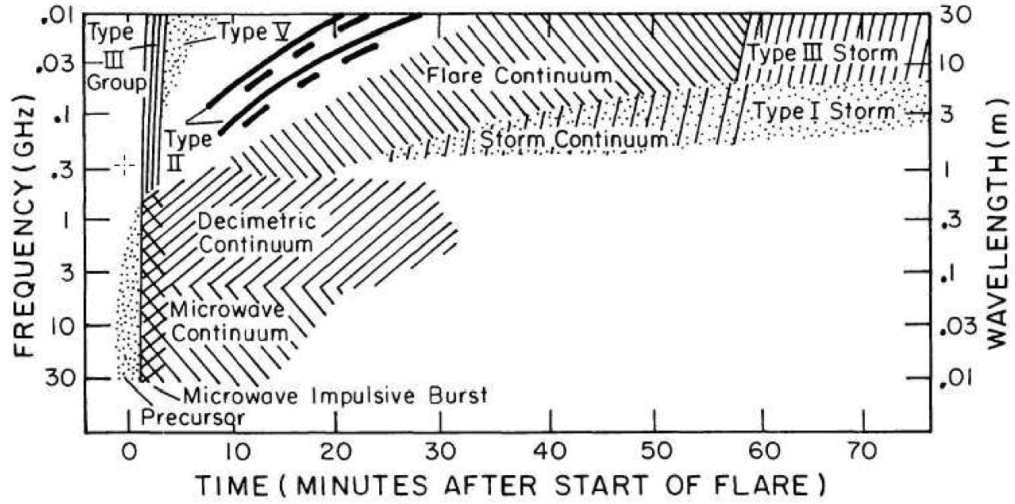


Figure 1.2: Schematic radio dynamic spectrum showing different types of solar radio bursts [4].

Table 1.3: Types of Solar Radio Bursts

Type	Characteristics	Duration	Frequency range
I	Short, narrow-bandwidth, occurs in large numbers with underlying continuum	Single bursts: 1 second, Storm: days	80-200 MHz
II	Slow frequency drifts, usually accompanied by a second harmonic	3-30 minutes	Fundamental: 20-150 MHz
III	Fast frequency drifts, can be accompanied by a second harmonic	Single bursts: 1-3 seconds, Group: 1-5 minutes, Storm: minutes-hours	10kHz - 1GHz

### 1.3.1 Type I

Type I bursts are a non-flare related phenomenon. They consist a continuum component called noise storm. The frequency range of this component is 100-400 MHz with variations on timescales of hours due to energetic electrons trapped on the closed coronal magnetic field lines. Another component is called burst component which is short and very narrow band. They tend to occur in drifting chains of 10-20 MHz. The absence of diagnostics at other wavelengths makes them difficult to study [3].

### 1.3.2 Type II

Type II bursts are characterized by slow frequency drifts and most being detected below 100 MHz. They occur at the time of soft X-ray peak in a solar flare and are accelerated in shocks in the corona. It is assumed that Type II bursts are associated with coronal shock wave accelerating electrons, driving Langmuir waves at the plasma frequency and its second harmonics [5].

## 1.4 Type III Bursts

Solar Type III radio bursts are characterized by fast frequency drifts from hundreds of MHz in the solar corona to tens of kHz in the interplanetary space. Their size, intensity, frequency, duration, etc vary burst to burst. They can be accompanied by second harmonics.

### 1.4.1 Frequency Extent

During large solar flares, the starting frequency of the Type III bursts can be in GHz range [6; 7; 8]. Some start at 10s or 100s of MHz. The stopping frequency is also varied as the starting frequency. Type III bursts can exist at high frequencies over 100 MHz. These are electron beams confined to the corona by a magnetic field. Some other Type III bursts can make it few 10s kHz or even below. Weaker radio bursts generally had higher stopping frequencies due to electron beam dilution or background density fluctuations [9; 10].

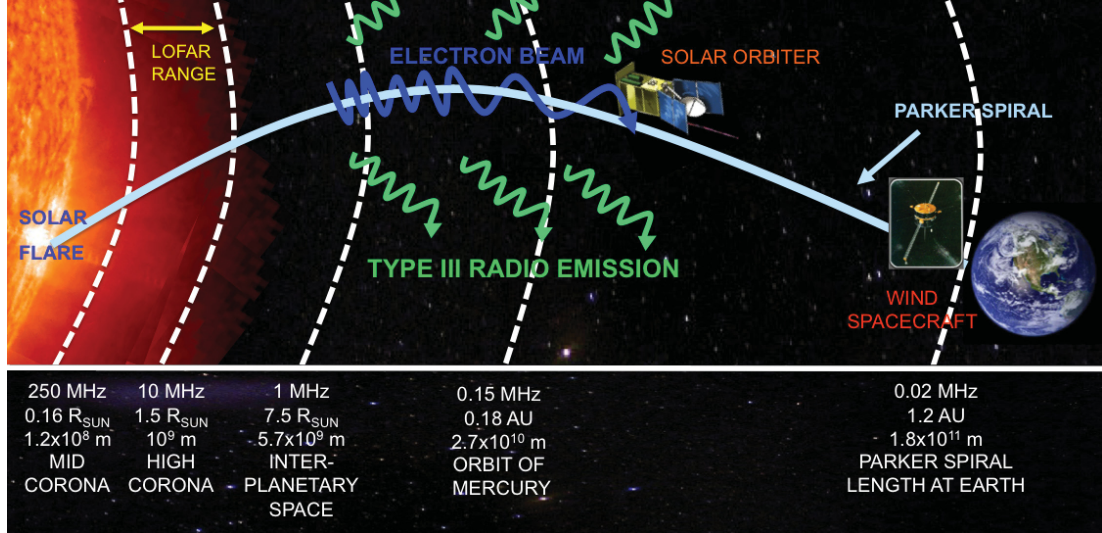


Figure 1.3: Type III radio bursts are created by electrons and can be observed in space and/or at Earth [6].

### 1.4.2 Burst Duration

Rise and decay times of Type III solar radio bursts are proportional to each other and both of them are roughly inversely proportional to the frequency. According to the statistical study of Evans et al. [11], rise time,  $t_r$  and decay time,  $t_d$  between 2.8 MHz and 67 kHz are  $4.0 \times 10^8 f^{-1.08}$  and  $2.0 \times 10^8 f^{-1.09}$  respectively, where  $t$  is in second and frequency  $f$  is in Hz [11]. Alvarez and Haddock used different frequency range from 200 MHz to 50 kHz and found a decay time  $t_d = 4.0 \times 10^{7.7} f^{-0.95}$  [12].

### 1.4.3 Frequency Drift Rate

Usually excited beam speeds for type III bursts are fractions of the light speed,  $c$  and can range from  $0.1c$  to  $0.6c$  [8; 13; 14; 15]. The drift rate of Type III bursts,  $df/dt$  is related to the speed of the exciting electron beam,  $v = dr/dt$ . Alvarez & Haddock reported  $df/dt = -0.01 f^{.84}$ . They used the rise time of Type III bursts between 3 MHz and 50 kHz [13]. Using radio bursts between 100 MHz and 3000 MHz Melendez et al. [8] found  $df/dt = 0.09 f^{.35}$  and Aschwanden et al. [16] reported  $df/dt = 0.1 f^{.4}$ . Ma et al. found a much faster frequency drift rate,  $df/dt = -2.6 \times 10^{-6} f^{2.7}$ , in the range 635 MHz to 1500 MHz [17].

#### 1.4.4 Source Flux

The peak source flux is directly proportional to the frequency in the corona up to 1 MHz and then it becomes inversely proportional [18; 19]. Some bursts were observed from 0.1 MHz to 5 MHz and some are found to start around 50 MHz and end at 20 kHz [20]. Saint-Hilaire et al. studied type III burst source fluxes at 450 MHz to 150 MHz and found a relation between normalization constant ( $A$ ) and frequency as  $A \propto f^{-2.9}$  [21].

#### 1.4.5 Source Size

The size of type III bursts changes inversely proportionally with frequency. From different measurements, the size is found 2' at 432 MHz, 4.5' at 150 MHz [21], 11' at 80 MHz, 20' at 43 MHz [22], 5' at 1 MHz, 50' at 100 kHz [23], and 1 AU at 20 kHz [24].

#### 1.4.6 Brightness

The brightness temperature  $T_b$  of Type III solar radio bursts are measured using flux density and source size. The value of  $T_b$  is high for Type III Bursts and typical value lie within the range  $10^6 K$  to  $10^{12} K$  [6]. The maximum brightness temperature  $T_b = 10^{15} K$  was observed by Suzuki and Dulk in 1985 [25]. Saint-Hilaire et al. investigated 10 years of NRH data and found brightness temperature varies as a power law with the spectral index around  $-1.8$  within the range 150–450 MHz [21]. At lower frequencies,  $T_b$  increases with the decreasing of frequency up to 1 MHz and then either decreasing or remaining constant.

#### 1.4.7 Harmonic Structure

Fundamental and harmonic components are seen in a large number of solar radio bursts at frequencies in the MHz and kHz ranges. Both fundamental and harmonic emissions are seen below 100 MHz, but above 100 MHz, the component is thought to be the harmonic [22; 25; 26; 27; 28]. The fundamental component is almost never seen above 500 MHz while the harmonic is only affected above 1

GHz [29]. The observed fundamental and harmonic ratio generally ranges from 1.5:1 to 2:1 [26; 27].

## 1.5 Fundamentals of Plasmas

The precise mechanism for the formation and propagation of solar radio bursts, specifically Type III bursts are still debated but plasma emission mechanism is now the generally accepted model. Before we investigate plasma emission mechanism, in this section we will first review some essentials of basic plasma physics.

### 1.5.1 Plasmas

The word ‘plasma’, comes from the Greek which means ‘moldable substance’ or ‘fabricated’, and first used by the Nobel Prize winning American chemist Irving Langmuir and his colleague Lewi Tonks in 1929 [30]. They noticed that under certain conditions, there is cohesiveness among the particles of ionized gas which is similar to the movement of red and white corpuscles of the blood plasma.

There are four states of matter in our universe namely solid, liquid, gas, and plasma. Plasma is regarded as the fourth state of matter. If we apply heat to a solid, generally it first changes to liquid and then liquid to gaseous. If we apply sufficient heat to the gaseous, outmost orbital electrons can overcome their binding energy and becomes an ionized gas. In natural gas, the interparticle force is of short range Vander Waals type. On the other hand, plasma is regarded as a statistical system composed of charged particles, mainly electrons, ions and dust particles and this force is long range Coulomb force in plasma. Each plasma particle can simultaneously interact with all other particles. Due to the long range coulomb forces, plasma exhibits collective behavior which is not found in natural gases.

It has been said that more than 99% of the matter in the visible universe is in the plasma state [31]. Generally, classical Plasmas are characterized by regimes

of high temperature and low density. Plasmas are found in space, earth's atmosphere, Van Allen radiation belts, solar wind, interplanetary and interstellar media as well as in laboratory gas discharges and thermonuclear fusion experiments. The dynamics of a plasma is governed by internal fields produced by the plasma particles and the externally applied fields [32].

### 1.5.2 Debye Shielding and Debye Length

Debye shielding is the ability of plasma to shield out electric fields that are applied to it. It is one of the fundamental and important phenomena of plasma and often called electrostatic Debye screening. To describe Debye shielding we consider a plasma of uniform number density  $n$  of both electrons and ions with mass  $m$  and electric charge  $e$ . Initially, there is no net electric charge or no electric field. Now we consider a test positive charge is introduced in the plasma. The positive test charge repels positively charged ions but attracts negatively charged electrons. Thus the test positive charge will be rapidly surrounded by a cloud of electrons situated in a sphere of radius  $\lambda_D$ . The sphere is called Debye sphere and the radius  $\lambda_D$  of the sphere is called Debye Length [31]. For  $T_e \gg T_i$ , the Debye length is governed by the ion temperature and is given by:

$$\lambda_D = \left( \frac{k_B T_i}{4\pi n e^2} \right)^{1/2}, \quad (1.1)$$

Where  $k_B$  is the Boltzmann constant and  $T_i(T_e)$  is the ion(electron) temperature. If we ignore ion motion, the Debye length expression takes the form:

$$\lambda_D = \left( \frac{k_B T_e}{4\pi n e^2} \right)^{1/2}. \quad (1.2)$$

Debye length is the scale over which mobile charge carriers screen out electric fields in plasma and it is a fundamental unit of length in plasma physics. The value of Debye length for solar core, solar wind, and magnetosphere are  $10^{-11}m$ ,  $10m$ , and  $100m$  respectively.

### 1.5.3 Plasma Frequency

When electrons in a uniform plasma are displaced from their equilibrium position against uniform background of ions, an electric field arises because of charge separation. This electric field creates a restoring force which tends to pull back the displaced electrons towards the excess positive charge. Because of the inertia, electrons will replenish the positive region and travel further away by generating a restoring electric field in the opposite direction. Thus the electrons oscillate about their equilibrium position and the system behaves as a harmonic oscillator. The oscillations are called plasma oscillations and the frequency of the oscillation is called plasma frequency [31]. The expression of the plasma frequency can be written as:

$$\omega_e = \left( \frac{4\pi n e^2}{m} \right)^{1/2}. \quad (1.3)$$

The relationship between plasma frequency and the Debye length is given by:

$$\lambda_D = \frac{v_T}{\omega_e} = \left( \frac{k_B T}{4\pi n e^2} \right)^{1/2}, \quad (1.4)$$

where  $v_T$  is the thermal speed of the electrons given by

$$v_T = \left( \frac{k_B T}{m} \right)^{1/2}. \quad (1.5)$$

### 1.5.4 Criteria for Plasma

There are three criterions for an ionized gas must satisfy to be called a plasma described below [31]:

- Linear dimension  $L$  of the plasma system must be much larger than the Debye length  $\lambda_D$ , i.e.,  $L \gg \lambda_D$  which means charges are able to shield out in a distance short compared with  $L$  leaving the bulk of plasma free of large potentials or fields. This condition ensures quasineutrality of the plasma.

- Debye shielding is statistically valid if there are enough particles in the sheath region, i.e., the number of particles in a Debye sphere ( $N_D$ ) must be very much greater than unity. ( $N_D$ )  $\gg$  1 is also called the collective behavior of the plasma.
- If  $\tau$  is the mean time between collisions of plasma particles with neutral atoms, the third criterion is given by  $\omega_e \tau > 1$ , where  $\omega_e$  is the frequency of typical plasma oscillation.

## 1.6 Plasma Waves

Evolution of time-dependent effects is common in plasma for many reasons. Generally, the plasma particles are in fast motion due to high temperature. Charges can move around and they can generate local concentrations of positive and negative charges (microscopic charge separations) which give rise to the electric fields. The motion of charges also generates current and hence magnetic fields. Therefore electric and magnetic fluctuations are typical in plasma. On the other hand, plasma reacts to any type of distortion of its state and can generate electric and magnetic fields in a similar way. Disturbance is thought as a superposition of linear waves onto the quiescent state which propagates throughout the plasma volume to transport energy of the distortion and is measured in many different frequencies [1]. In order to generate plasma waves, any disturbance must be a solution of the appropriate equations of the plasma. Also, amplitude of the disturbance must be higher than the thermal fluctuations. One of the ways to study wave propagation in plasma is to solve plasma fluid equations along with Maxwell's equation and thus find a relation between wave number  $k$  and wave frequency  $\omega_e$ . This relation is called dispersion relation and all information regarding wave propagation can be obtained from it. Plasma can be characterized as a medium having a conductivity or a dielectric constant and the wave equation can be derived using Maxwell's equation. This is the second approach to study plasma waves [30].

### 1.6.1 Electron Plasma Waves

Let us consider an unmagnetized collisionless warm plasma containing electrons and ions. Electrons have their thermal velocities and react differently to displace them from their equilibrium positions. To treat this effect, a scalar pressure term is needed to add to the equation of motion and the plasma oscillation of such plasma is called plasma wave or Langmuir wave. The dispersion relation for the electron-acoustic wave can be written as the following expression [31]

$$\omega^2 = \omega_e^2 + 3kv_T^2, \quad (1.6)$$

where  $k$  is the wave number and  $v_T$  is the electron thermal velocity given by expression (1.5). This equation is also known as Langmuir wave dispersion relation. Eq. (1.6) can be written in terms of Debye length as follows

$$\omega^2 = \omega_e^2(1 + 3k^2\lambda_D^2). \quad (1.7)$$

From Eq.(1.7), it is clear that the thermal perturbation becomes important when  $k\lambda_D \sim 1$ , i.e., the wavelength of perturbation  $\sim \lambda_D$ . For long period plasma waves, where  $k$  goes to zero, there is a natural oscillation at the electron plasma frequency,  $\omega \sim \omega_e$ .

### 1.6.2 Ion-Acoustic Waves

Langmuir waves are high frequency electron oscillations where the contribution of ions is neglected. At lower frequencies, ion inertia is important, and can not be neglected. In this case, electron inertia can be neglected because of very low mass compared to ion mass. Dispersion relation of an ion-acoustic wave is given by

$$\omega = kv_s, \quad (1.8)$$

where,  $v_s = [(k_B T_e + \gamma_a k_B T_i)/m_i]^{1/2}$  is the ion-acoustic speed or sound speed in plasma and  $\gamma_a$  is the adiabatic constant.

### 1.6.3 Electromagnetic waves

As we discussed before, the motion of the charge particles generates plasma current and hence magnetic field which is the source of the electromagnetic wave modes. Many types of electromagnetic waves can propagate in a magnetized plasma. In an unmagnetized plasma, the simplest electromagnetic mode is the free-space electromagnetic wave. The dispersion relation of such a wave is given by

$$\omega^2 = \omega_e^2 + c^2 k^2, \quad (1.9)$$

where  $c$  is the speed of light in vacuum.

# Chapter 2

## Motivation and Approach

### 2.1 Motivation

As we discussed in previous chapter, the Sun is the most efficient and prolific particle accelerator in our solar system. Solar flares release energy on the order of  $10^{32}$  erg and accelerate up to  $10^{36}$  electrons per second in the solar atmosphere [33]. Solar storms and electromagnetic bursts are the solar activity related to the flares. Solar radio bursts are classified by how their frequency changes in time, called the frequency drift rate. Solar type III radio bursts are characterized by fast frequency drifts from hundreds of MHz in the solar corona to tens of kHz in the interplanetary space. They can be accompanied by second harmonics. Bursts are an important diagnostic tool in the understanding of solar accelerated electron beams. They provide information on electron acceleration and transport, and the conditions of the background ambient plasma they travel through. Figure 2.1 shows STEREO/WAVES satellite observation of a local type III burst [34]. Since fast drifting emission frequency depends on the frequency of Langmuir waves, it occurs at a lower frequency when electron density decreased at a later time. Non-drifting emissions are Langmuir waves excited probably by beam electrons. The problem of generation of electromagnetic radiation at the plasma frequency and its second harmonic at beam-plasma interaction is one of the most intensively studied topics in plasma physics, experimentally and theoretically as well [35]. Up to now, there is the general consensus which goes back

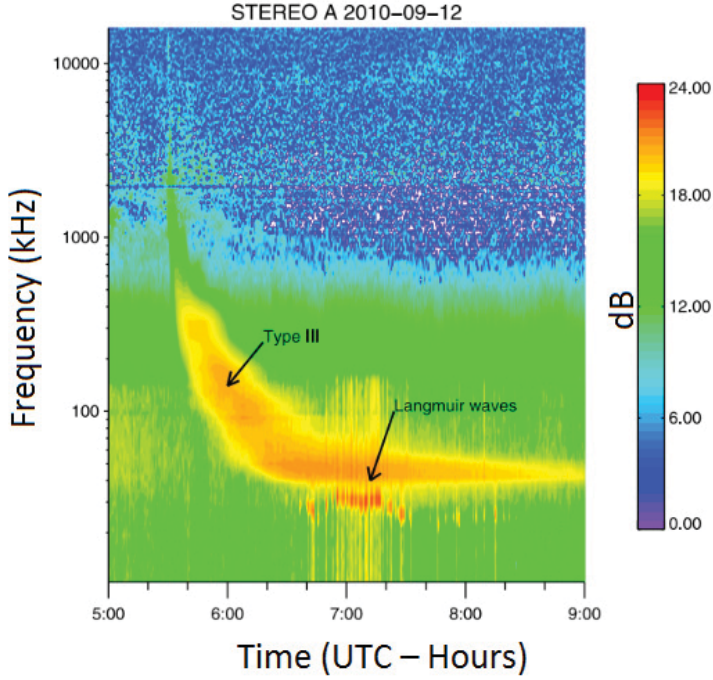


Figure 2.1: Dynamic spectrum of a local type III radio burst (fast drifting emission from 5 MHz down to 30 kHz) and associated Langmuir waves (non-drifting emissions in the frequency interval 27-32 kHz [34]).

to papers of the sixties by Ginzburg and Zhelesniakov [36] that second harmonic generation is accomplished in two steps: (1) electron beams develop bump-on-tail distributions and excite Langmuir waves at the local electron plasma frequency,  $\omega_e$  and (2) nonlinear interaction of Langmuir waves leads to the generation of electromagnetic waves at  $\omega_e$  as well as second harmonics at  $2\omega_e$ .

Figure 2.2 shows the evolution of a beam in the tail of a thermal distribution, starting with the arrival of the fastest electrons at time  $t_1 = L/v_1$ , producing a positive slope  $\partial f / \partial v > 0$  and becomes unstable. At later times, slower electrons arrive at  $t_2 = L/v_2$  and  $t_3 = L/v_3$ , but the slowest ones do not produce a positive slope and are stable. The velocity dispersion allows higher energy electrons to race ahead of the lower energy electrons and creates a so-called bump or beam in the forward direction of the particle distribution function [37]. Landau resonance with the unstable electron beam generates Langmuir waves. Nonlinear wave-wave interactions produce electromagnetic emissions at the local electron plasma frequency and its second harmonic, generally called type III radio bursts. Langmuir waves lose energy which causes the accelerated electron stream to decelerate and

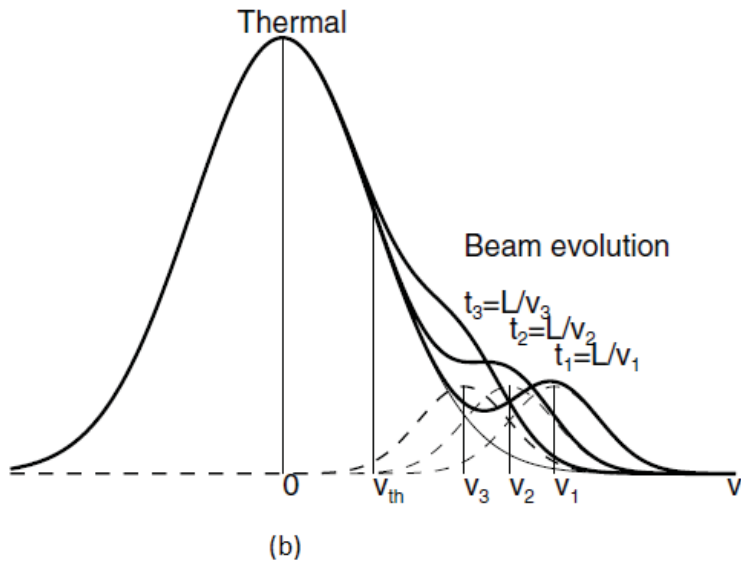


Figure 2.2: Bump-on-tail distributions [37].

decay processes are suppressed due to fast beam stabilization. Therefore, the waves can not survive over the long distance like 1 AU (Sun to Earth). From different space observations, it is obvious that Type III radiation can propagate a long distance, even beyond 1 AU which creates a conflict known as the Sturrock dilemma [38]. Different attempts to find a way out of this dilemma [39; 40] remained, however, unsatisfactory until now.

An electron beam can escape the quasi-linear relaxation and travel over large distances if there is an effective disruption of the resonance between the Langmuir waves and the beam. An electrostatic decay of Langmuir waves into daughter Langmuir and ion acoustics waves can remove the Langmuir waves out of resonance with the beam by scattering them from resonance regions toward lower wave numbers. This theory is proposed by Kaplan and Tsytovich [41] and supported by type III radio bursts observations [42; 43]. As the estimated Langmuir waves are very intense some authors argued for strong turbulence processes e.g., oscillating two stream instability (OTSI), Modulational instability (MI) [39; 44], soliton formation, and Langmuir collapse [45], etc. These can pump the Langmuir waves toward higher wave numbers  $k_L$  at a much faster rate. It is considered as the most effective beam stabilization mechanisms. In the strong turbulence process, ion acoustics waves of frequency and wave number  $(f_1, k_1)$  can beat with two of the beam-resonant Langmuir waves with frequencies and wave numbers

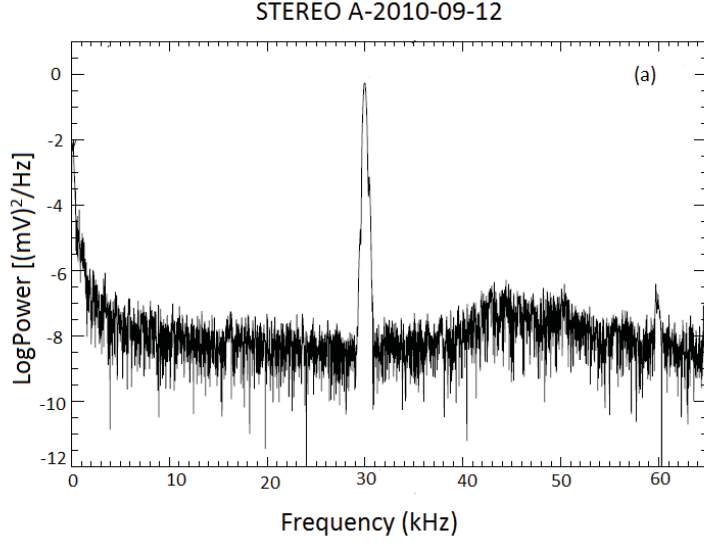


Figure 2.3: The spectrum observed during the type III event by the Time Domain Sampler [34]

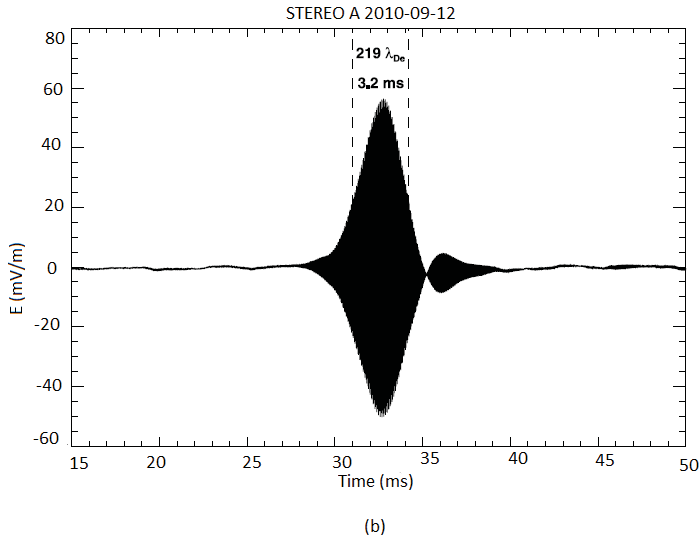


Figure 2.4: Langmuir wave packet observed during the type III event by the Time Domain Sampler [34].

$(f_2, k_2)$ . They produce two oppositely propagating upshifted and downshifted high frequency sidebands in the non resonant region with frequencies and wave numbers  $(f_2 - f_1, k_2 - k_1)$  (Stokes mode) and  $(f_2 + f_1, k_2 + k_1)$  (anti-Stokes mode). The nonlinear effect of this process is responsible for the formation of the Langmuir envelope soliton-caviton pairs [46] and was observed by Voyager as a possible evidence for the Modulational instability and the spatial collapse of

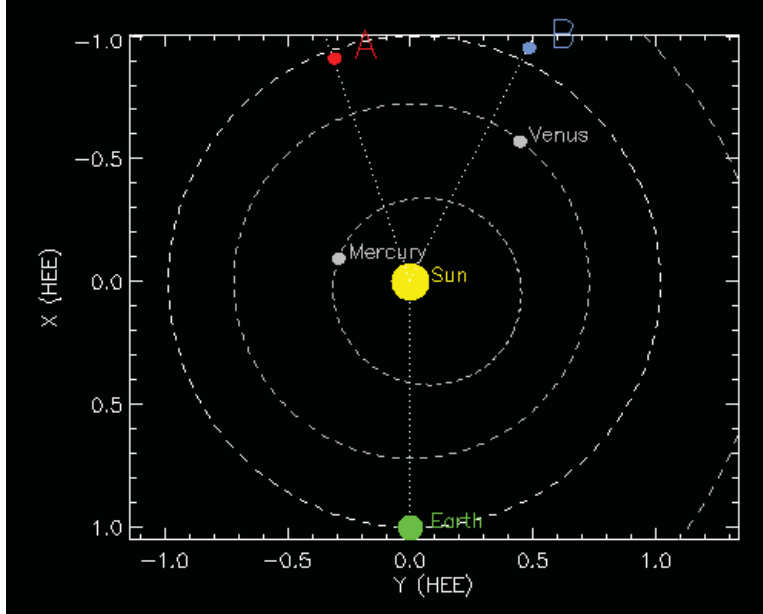


Figure 2.5: Positions of STEREO A and B for 23-Nov-2016 21:00 UT [stereo-ssc.nascom.nasa.gov/where.shtml].

Langmuir waves [47]. When the wave packet intensity is more than the threshold value, ponderomotive force and self-focusing can overcome linear dispersion and lead to collapse to produce electromagnetic waves at the plasma frequency and second harmonic [48]. Thejappa et al. [34; 49; 50; 51; 52] investigated several observations obtained by the WAVES experiment of the STEREO spacecraft in solar type III radio bursts and showed that Langmuir waves excited by the electron beams occur as localized wave packets with durations less than 10 ms, and the peak intensities well exceed the supersonic Modulational instability thresholds (see Fig 2.3 and 2.4). Their findings indicate that beam stabilization as well as conversion of Langmuir waves into escaping radiation at the fundamental and second harmonic of the electron plasma frequency can be described with the help of the supersonic Modulational instability and the spatial collapse.

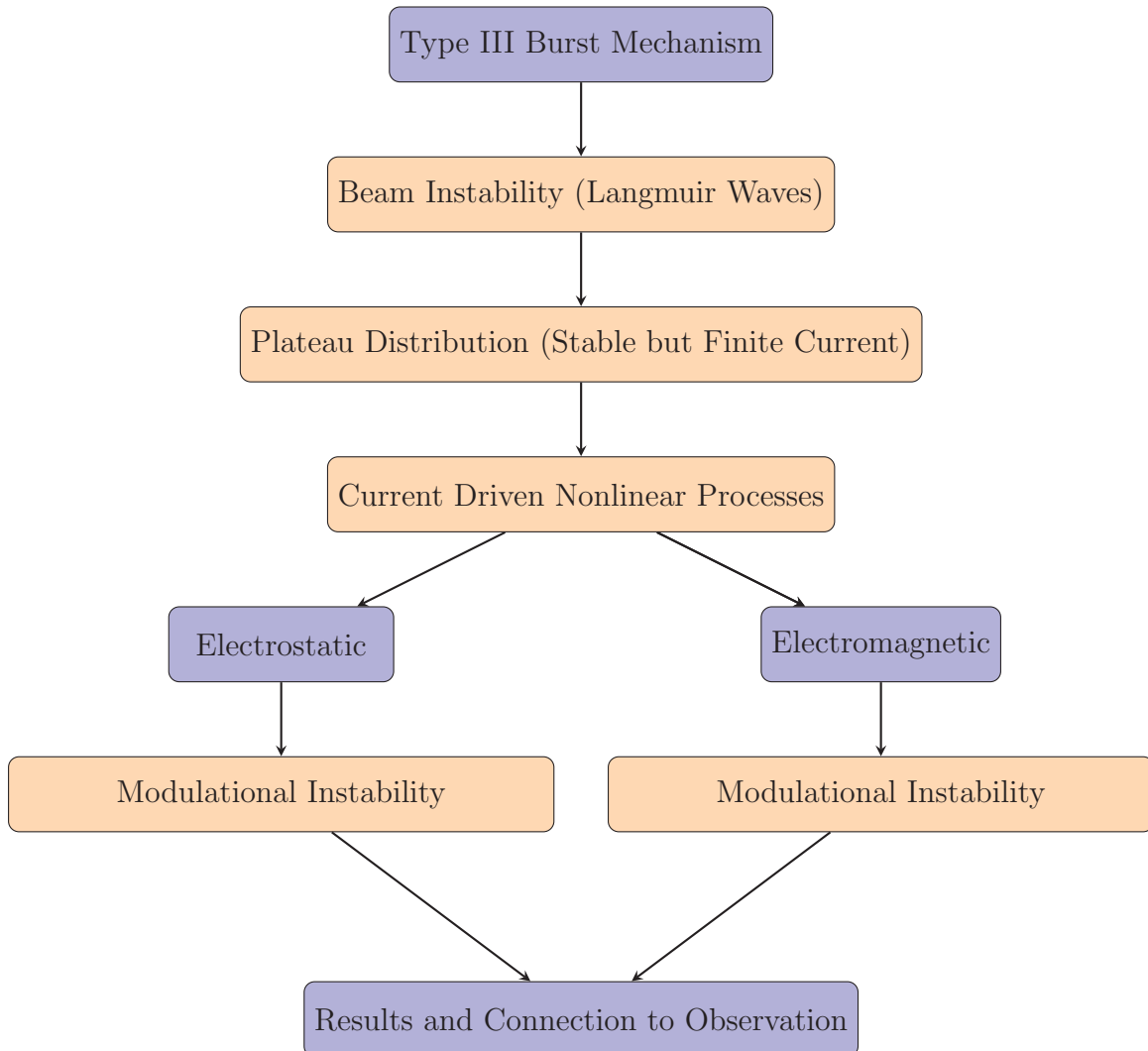
On the other hand, Graham et al. [53; 54] investigated the same STEREO events as Thejappa et. al. [34; 49; 50; 51; 52], but found different results. Their analysis showed that none of the wave packets are consistent with collapse and they did not find evidence of modulational instability. This is because Langmuir wave packets have field strengths too small for collapse to proceed. Thus all the mechanisms that have been proposed in the literature are controversial and are not sufficient to solve the problem of generation and survival of plasma radiation over long

distances. Very recently Sauer and Sydora [55; 56] introduced a new technique to describe Langmuir oscillations at the plasma frequency with wave number  $k=0$ . This is different than the concept of beam-driven Langmuir waves which undergo parametric decay into ion acoustic wave and backscattered waves. They showed that saturation process of the beam instability is accompanied by the formation of a plateau distribution and the saturation state represents a current which can drive homogeneous electric field oscillations at the plasma frequency without any electrostatic instability. They used Ampere’s law instead of Poisson’s equation to describe this mechanism of current drive in the plasma. In this case, instead of beam-excited waves of finite wave number, Langmuir oscillations ( $\omega = \omega_e$ ,  $k = 0$ ) acts as a specific pump wave for the modulational instability. Thus this model gives a possible alternative explanation to resolve the controversy between Graham et al. [53; 54] and Thejappa et al. [34; 49; 50; 51; 52]. However, both electrostatic and electromagnetic linear and nonlinear effects can be studied by current driven oscillations. Investigation of Sauer and Sydora [55; 56] is limited to only electrostatic case. To the best of our knowledge, no investigation has been done to explain the mechanism of electromagnetic radiation and their harmonics in the form of type III radiation. Therefore, in the present study, we have investigated mechanisms to solve this problem by considering the occurrence of current-driven Langmuir oscillations in plasmas with plateau distributions. We have found that the capability of driving Langmuir oscillations after the beam has saturated, associated with the wave packet formation via modulational instability, offers a simple mechanism to explain long-lasting type III emission. We have made dispersion analysis from linear theory and kinetic (particle-in-cell) electromagnetic simulations for nonlinear electrostatic and electromagnetic processes.

## 2.2 Overview of Approach

In this thesis, we first introduce fundamentals of the solar wind and basic plasma parameters in Chapter 1. In Chapter 2, we describe our motivation and methodology of the study. In Chapter 3, we present linear dispersion theory analysis based on local plasma parameters. Chapter 4 is the discussion of particle-in-cell (PIC) models which are then used to study kinetic simulations for nonlinear electrostatic and electromagnetic process in Chapter 5. Finally, in Chapter 6, we present the summary and limitations of our present study and propose future works.

## Flowchart of our approach of investigation



# Chapter 3

## Linear Analysis

### 3.1 Introduction

The problem of electron-beam-plasma interactions is one of the most fundamental processes in space plasmas and plasma instabilities play an important role in many astrophysical phenomena especially plasmas associated with solar wind, sun spot, Van Allen radiation belts, pulsars, etc [30]. It is well known that electron beam instabilities develop into nonlinear waves and turbulence. In this chapter, in order to clarify the mechanism of Langmuir waves modulation, we first analyze the linear stability properties of plasmas with a weak electron beam. We describe a mode for electron beams and make a stability analysis from the dispersion relation derived by linear analysis. We make numerical solutions to the dispersion relation and discuss the results for different plasma parameters.

### 3.2 Electron Beams

An ordered flow as charged particles such as electrons or ions, or a mixture of them, is referred to a beam. A thermal plasma which is not ordered is not a beam. The mixture of plasma particles (usually electrons and ions) is space-charge neutralized and the particles are governed by long-range electromagnetic interactions. When high current beam enters a plasma, they generate an electric field. The plasma particles move to cancel the beam generated electric field. Response of plasma due to incoming beams depends on the kinetic energy of the plasma particles and it provides complete neutralization of the beam space charge and current. High current pulsed electron beams can cause large electron

drift velocity which is responsible for two-stream instability and rapid plasma heating. The study of the possibility of long distance propagation of electron beams through the atmosphere is very important to understand space weather. Beam plasma can be generated by low-energy electron discharges, laser ionization, pulsed plasma guns, collisions of beam particles with a background gas, etc [57].

### 3.3 Plasma Wave Instability

#### 3.3.1 Instability in Plasma

Stability of plasma is a very important field of plasma physics. In some cases, if the plasma is not in thermodynamic equilibrium, a collective mode may become unstable. When small changes in the characteristics of a plasma (e.g. temperature, density, electric fields, magnetic fields) lead to large effect on them and change the property of the plasma drastically then we call it plasma instability. Completely stable plasmas are not common in nature because most of the plasmas are far from thermodynamic equilibrium. Due to the influence of external fields, flows of particles, momentum, and energy can be created. The level of the fluctuations affects the rates of transport processes in the plasma. Mathematically, general solution of any dispersion relation can be split into two parts as follows

$$\omega = \omega_r + i\gamma, \tag{3.1}$$

where  $\omega_r$  is the real part and  $\gamma$  is the imaginary part of the angular frequency. The imaginary part of the angular frequency,  $\gamma$  determines the existence and non-existence of waves in plasma. If  $\gamma$  is negative, the plasma is stable against the excitation. On the other hand, when  $\gamma$  is positive, the plasma wave grows exponentially and the perturbation is unstable [1; 31; 58]. In some situations, a wave can extract energy from the system by drawing kinetic energy from pre-existing motion or potential energy from background stratification. In both cases, the wave amplitude grows over time and becomes unstable. When electrons have a velocity close to the phase velocity, they experience a stationary field and strongly interact with the field. If the electron velocity is small compare

to the phase velocity then they are pushed by the wave and are continuously accelerated. On the other hand, electrons push the wave and are decelerated when their velocity is larger than the phase velocity. In Maxwellian distribution, there are more electrons traveling slower than the wave and the electrons gain energy from the wave. As a result, the wave loses energy to the electrons and its amplitude decreases with time. Because there is no free energy in Maxwellian distribution, there is no instability. In a nonuniform plasma, pressure gradient provides free energy for low frequency mode.

### 3.3.2 Instability in Cold Beam Plasma

Through beam-plasma interaction, electron plasma mode can be easily excited by an electron beam. Let us consider a plasma of cold electrons and a monochromatic beam of charged particles is injected into it. The distribution function can be written as

$$f = (n_0/n)\delta(v) + (n_b/n)\delta(v - v_b), \quad (3.2)$$

where  $v_b$  is the beam velocity and  $n_0$  and  $n_b$  are the densities of the cold electrons and beam electrons [58]. As described earlier, strong interaction between the beam and background electrons occurs when the velocity of beam electron  $V_b$  is nearly equal to the phase velocity, i.e., when  $kv_b = \omega_e$ . Here  $\omega_e$  is the electron plasma frequency. When the beam electrons give away energy to the electron plasma wave, the wave grows exponentially in the time with the rate

$$\gamma_{max} = \frac{\sqrt{3}}{2} \left( \frac{n_b}{2n_0} \right)^{1/3} \omega_e. \quad (3.3)$$

## 3.4 Water-bag Distribution

A beam can be heated by wave-plasma interaction and becomes broader in the direction of smaller velocities. Thus beam thermal velocity increases and its drift velocity decreases. This phenomenon can be illustrated by using water-bag distributions as shown in figure 3.1. It shows the distribution functions at 4 times during the evolution of beam-plasma interaction, starting from the initial beam

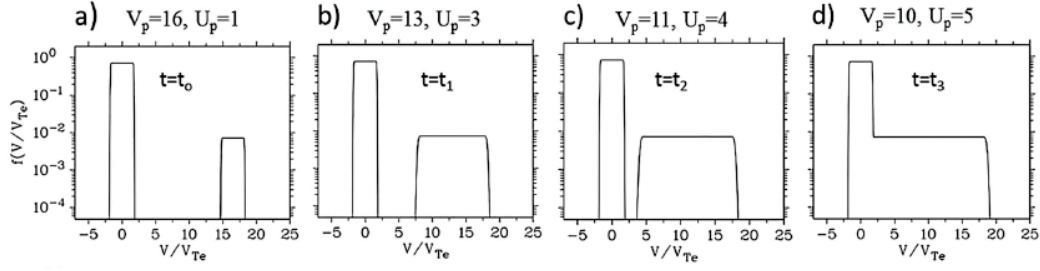


Figure 3.1: Distribution function versus velocity normalized to thermal speed shows the transition from (a) pronounced beam instability to (d) a stable state.[55].

( $t = t_0$ ) up to the formation of a full plateau ( $t = t_3$ ). The gap in velocity space between the beam and the main plasma diminishes in time up to saturation. In saturation, the beam instability is completely quenched and a plateau distribution is formed [55].

### 3.5 Model Fluid Equations

We consider a simplified beam plasma system where the wave propagates in the  $x - z$  plane along the  $x$ -axis, two additional electromagnetic field components,  $E_z$  and  $B_y$ , can be driven by the  $x$ - and  $z$ - components of the electron beam velocity,  $v_{px} = V_p \cos \theta$ ,  $v_{pz} = V_p \sin \theta$ , where  $\theta$  is the angle between the  $x$ - axis and the direction of the streaming plasma and  $V_p$  is the beam velocity. Figure 3.2 shows the schematic of the electromagnetic beam plasma system under consideration.

We can consider our plasma system as a simple one-dimensional box of length  $L$  having an electron plasma (index “e”) at rest with density  $n_{e0}$  and thermal speed  $V_{Te} = (kT_e/m_e)^{1/2}$ . The box is continuously filled by the incoming beam(plateau) plasma (index “p”) of density  $n_{p0}$ , and initial thermal speed  $V_{Tp} = (k_B T_p/m_e)^{1/2}$ ,  $m_e$  being the electron rest mass,  $k_B$  is the Boltzmann constant,  $T_e(T_p)$  is the temperature of the main (beam) plasma component. Ions are taken as immobile forming the charge-neutralizing background. The complete system which describes the coupling between electrostatic and electromagnetic fields consists of nine equations for the fluid variables  $n_e, v_{ex}, v_{ez}, n_p, v_{px}, v_{pz}$  and the electromagnetic components  $E_x, E_z$  and  $B_y$  which are written as

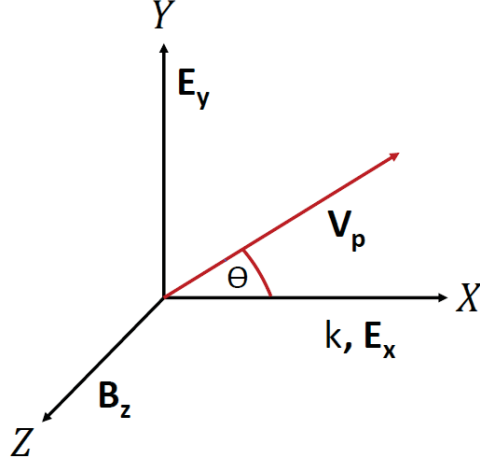


Figure 3.2: Schematic of the electromagnetic beam plasma system.

- Continuity equation and equations of motion for the main plasma:

$$\frac{\partial}{\partial t} n_e + \frac{\partial}{\partial x} (n_e v_{ex}) = 0, \quad (3.4)$$

$$\frac{\partial}{\partial t} v_{ex} + v_{ex} \frac{\partial}{\partial x} v_{ex} + \gamma_a \frac{1}{n_e} \frac{\partial}{\partial x} n_e = -(E_x - \frac{v_{Te}}{c} v_{ez} B_y), \quad (3.5)$$

$$\frac{\partial}{\partial t} v_{ez} + v_{ex} \frac{\partial}{\partial x} v_{ez} = (E_z + \frac{v_{Te}}{c} v_{ex} B_y), \quad (3.6)$$

- Continuity equation and equations of motion for the plateau plasma:

$$\frac{\partial}{\partial t} n_p + \frac{\partial}{\partial x} (n_p v_{px}) = 0, \quad (3.7)$$

$$\frac{\partial}{\partial t} v_{px} + v_{px} \frac{\partial}{\partial x} v_{px} + \gamma_a V_p^2 \frac{1}{n_p} \frac{\partial}{\partial x} n_p = -(E_x - \frac{v_{Te}}{c} v_{pz} B_y), \quad (3.8)$$

$$\frac{\partial}{\partial t} v_{pz} + v_{px} \frac{\partial}{\partial x} v_{pz} = -(E_z + \frac{v_{Te}}{c} v_{px} B_y), \quad (3.9)$$

- Ampere's and Faraday's law:

$$\frac{\partial}{\partial t} E_x = n_e v_{ex} + \mu n_p v_{px}, \quad (3.10)$$

$$\frac{\partial}{\partial t} E_z - \frac{c}{v_{Te}} \frac{\partial B_y}{\partial x} = n_e v_{ez} + \mu n_p v_{pz}, \quad (3.11)$$

$$\frac{\partial}{\partial t} B_y - \frac{c}{v_{Te}} \frac{\partial E_z}{\partial x} = 0, \quad (3.12)$$

where  $n_e$  ( $n_p$ ) is the main(plateau) electron density normalized to its equilibrium

value  $n_{e0}$  ( $n_{p0}$ ),  $v_{ex}$  ( $v_{ez}$ ) is the electron fluid speed along  $x(z)$ - direction normalized to the thermal speed  $v_{T_e} = (kT_e/m_e)^{1/2}$  of main population,  $U_p = T_p/T_e$ , density ratio  $\mu = n_{p0}/n_{e0}$  and the adiabatic constant  $\gamma_a = 1.5$ . The time variable ( $t$ ) is normalized to the reciprocal plasma frequency  $\omega_e^{-1} = (\epsilon_0 m_e / n_{e0} e^2)^{1/2}$  with  $e$  being the magnitude of the charge of an electron, and space variable ( $x$ ) is normalized to the Debye length  $\lambda_D = v_{T_e} / \omega_e$ . The electric field amplitude  $E$  is normalized to  $E_0 = (m_e / e) \omega_e v_{T_e}$ . The magnetic field is written in units of  $B_0 = E_0 / c$  where  $c$  is the speed of light.

### 3.6 Derivation of the Dispersion Relation

Using Eqs. (3.4)-(3.21) we will derive a dispersion relation and discuss a simple dispersion theory to illustrate the transition from an unstable beam to a stable state. From a solution of the dispersion relation the characteristics of this transition will be described. To obtain dispersion relation we consider small-amplitude assumption and expand variables  $n_e$ ,  $v_{ex}$ ,  $v_{ez}$ ,  $n_p$ ,  $v_{px}$ ,  $v_{pz}$ ,  $E_x$ ,  $E_z$  and  $B_y$  in power series of  $\epsilon$  as follows

$$n_e = 1 + \epsilon n_e^{(1)}, \quad (3.13)$$

$$n_p = 1 + \epsilon n_p^{(1)}, \quad (3.14)$$

$$v_{ex} = 0 + \epsilon v_{ex}^{(1)}, \quad (3.15)$$

$$v_{ez} = 0 + \epsilon v_{ez}^{(1)}, \quad (3.16)$$

$$v_{px} = 0 + \epsilon v_{px}^{(1)}, \quad (3.17)$$

$$v_{pz} = 0 + \epsilon v_{pz}^{(1)}, \quad (3.18)$$

$$E_x = 0 + \epsilon E_x^{(1)}, \quad (3.19)$$

$$E_z = 0 + \epsilon E_z^{(1)}, \quad (3.20)$$

$$B_y = 0 + \epsilon B_y^{(1)}, \quad (3.21)$$

where  $\epsilon$  is a small parameter measuring the weakness of the dispersion. After taking Fourier transformation and lowest power of  $\epsilon$ , Eqs. (3.4)-(3.21) gives

$$n_e^{(1)} = \frac{k}{\omega} v_{ex}^{(1)}, \quad (3.22)$$

$$n_p^{(1)} = \frac{k}{\omega - kv_{px}} v_{px}^{(1)}, \quad (3.23)$$

$$v_{ex}^{(1)} = \frac{-i\omega}{\omega^2 - k^2\gamma U_e^2} E_x^{(1)}, \quad (3.24)$$

$$v_{ez}^{(1)} = \frac{-i}{\omega} E_z^{(1)}, \quad (3.25)$$

$$B_y^{(1)} = \frac{-kc}{\omega v_{Te}} E_z^{(1)}, \quad (3.26)$$

$$v_{px}^{(1)} = \frac{-i(\omega - kv_{px})}{(\omega - kv_{px})^2 - k^2 U_p^2 \gamma} (E_x^{(1)} + \frac{kv_{pz}}{\omega} E_z^{(1)}), \quad (3.27)$$

$$v_{pz}^{(1)} = \frac{-i}{\omega} E_z^{(1)}. \quad (3.28)$$

In Fourier transformation, we assumed that the perturbation is proportional to  $e^{ikx-i\omega t}$ , where  $k$  is the wave number,  $\omega$  is the angular frequency, and  $i$  is the imaginary number. Using Eqs. (3.22)-(3.28) in Eq. (5.1), we have

$$E_x^{(1)} = \frac{\mu kv_{pz}}{A_1 A_2 \omega} E_z^{(1)}, \quad (3.29)$$

where

$$A_1 = (\omega - kV_p \cos\theta)^2 - \gamma k^2 U_p^2, \quad (3.30)$$

$$A_2 = 1 - \frac{1}{\omega^2 - \gamma k^2 U_e^2} - \frac{\mu}{A_1} \quad (3.31)$$

$$\mu = \frac{n_{po}}{n_{eo}} \quad (3.32)$$

Combination and linearization of Eq. (3.11) and Eq. (3.29) leads to the following dispersion relation

$$1 - \frac{1 + \mu + (c/v_{Te})^2 k^2}{\omega^2} - \frac{\mu k^2 V_p^2 \sin^2\theta}{\omega^2 A_1} - \frac{\mu^2 k^2 V_p^2 \sin^2\theta}{\omega^2 A_1^2 A_2} = 0. \quad (3.33)$$

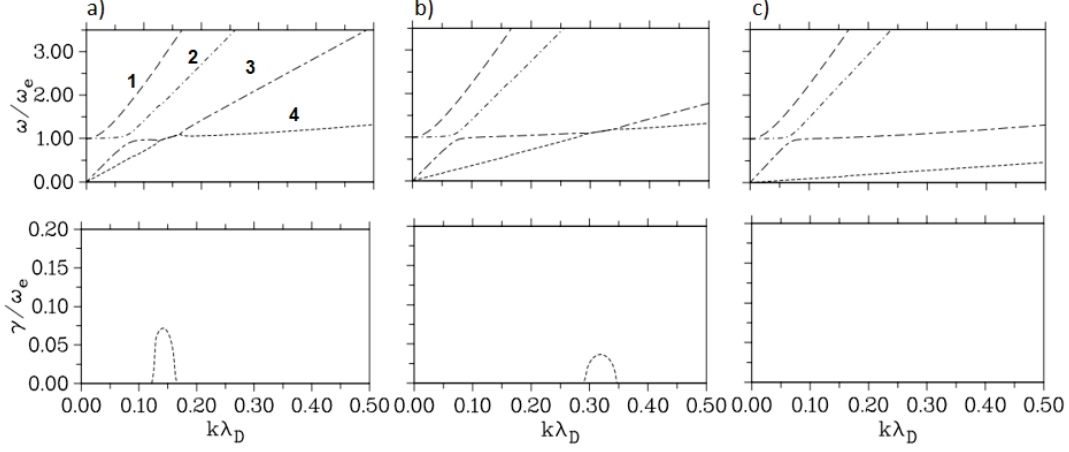


Figure 3.3: Sketch of the transition from a) pronounced beam instability to c) a saturated stable state, where  $\mu = n_{po}/n_{eo} = 0.01$ ,  $\theta = 30^\circ$ ,  $c/V_{Te}=0.05$  and parameters a) beam velocity  $V_p = 12$ , and thermal velocity  $U_p = 2$ . (b)  $V_p = 10$ ,  $U_p = 3$ , and (c)  $V_p = 9$ ,  $U_p = 4$ .

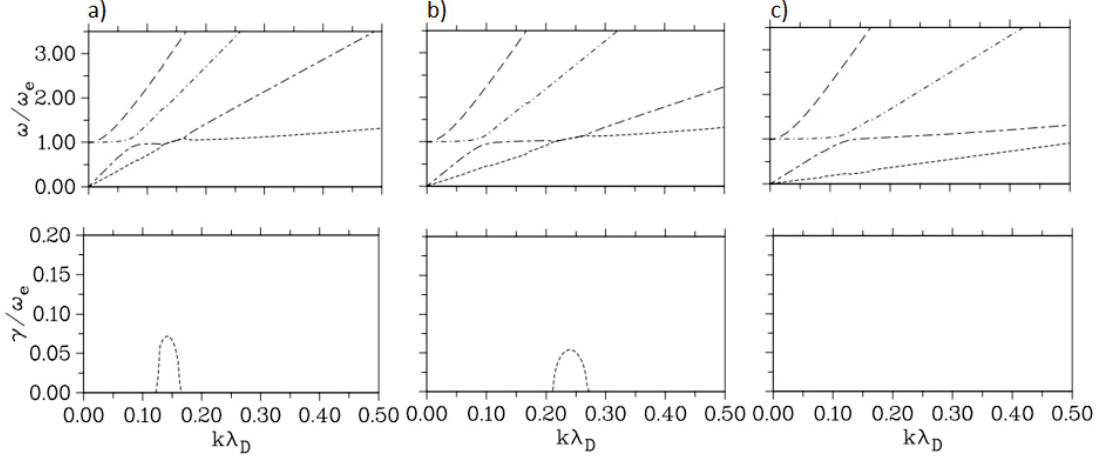


Figure 3.4: Sketch of the transition from a) pronounced beam instability to c) a saturated stable state, where  $\mu = n_{po}/n_{eo} = 0.01$ , beam velocity  $V_p = 12$ , thermal velocity  $U_p = 1$ ,  $c/V_{Te}=0.05$  and a)  $\theta = 30^\circ$ , (b)  $\theta = 50^\circ$ , and (c)  $\theta = 65^\circ$ .

### 3.7 Dispersion Analysis

The saturation of the beam instability can be studied from the solution of the dispersion relation given in Eq. 3.33 [35; 59; 60; 61]. To illustrate the properties of the beam instability we first solve the dispersion relation by calculating the coefficients of the polynomial. Results from the solution of Eq. 3.33 are represented in figures 3.3-3.6. Lower velocity side of the beam has a positive velocity gradient which causes resonance between the velocity of beam electrons with the phase

velocity of the waves and this resonance can excites Langmuir waves. Due to the wave-plasma interaction, beams are heated and beam becomes broader in the direction of smaller velocities. This means an enhancement of the beam thermal velocity and a reduction of its drift speed. Plateau distribution is formed when the gap in velocity space between the beam and the main plasma diminishes in time up to saturation. Figure 3.3 shows the transition from the onset of beam instability up to saturation form. The top panels of Figure 3.3 show the dispersion relations of the various modes ( 1. ordinary mode, 2. Langmuir mode, 3. modified electron acoustic mode, and 4. beam mode). The bottom panels are the imaginary part of the frequency of growth rate of the beam instability corresponding to the upper panel. This figure shows the transition from a) pronounced beam instability to c) a saturated stable state, where density ratio,  $\mu = n_{po}/n_{eo} = 0.01$ , the angle between the x-axis and the direction of the streaming plasma,  $\theta = 30^\circ$ ,  $c/V_{Te}=0.05$  and parameters a) beam velocity  $V_p = V_{Dp}/V_{Te} = 12$ , and thermal velocity  $U_p = V_{Tp}/V_{Te} = 2$ . (b)  $V_p = 10$ ,  $U_p = 3$ , and (c)  $V_p = 9$ ,  $U_p = 4$ . From Figure 3.3(a-c), it is clearly seen that during the transition from maximum beam instability to full plateau formation the maximum growth rate of the beam instability goes down and shifts to larger wave numbers. The wavenumber of maximum instability is initially at  $k\lambda_D \sim 0.17$ , it becomes nearly 0.3 just before the beam saturates. During this process, the related frequency changes from  $\omega \leq \omega_e$  to  $\omega \geq \omega_e$ . The top most wave mode is the light branch which is due to the consideration of the electromagnetic waves. It has been also found that there is no significant change in the ordinary mode due to the change of the beam velocity and thermal velocity.

Figure 3.4 shows the transition from pronounced beam instability to saturated state due to the changes of the angle  $\theta$  between the x-axis and the direction of the streaming plasma. It has been found that saturation state occurred when the value of  $\theta$  is about 65 for  $\mu = 0.01$ , beam velocity  $V_p = 12$ , thermal velocity  $U_p = 1$ ,  $c/V_{Te} = 0.05$ . Also, the maximum growth rate of the beam instability goes down and shifts to larger wave numbers as  $\theta$  increases. The wavenumber of maximum instability is initially at  $k\lambda_D \sim 0.16$ , it becomes nearly 0.27 just before the beam saturates. The light wave mode is not changing with the change of angle, but Langmuir wave mode shifts towards the larger wave number. Figure 3.5 shows the change of wave modes and maximum growth rate of the beam instability with the change of main to beam electron density ratio,  $\mu$ . From this

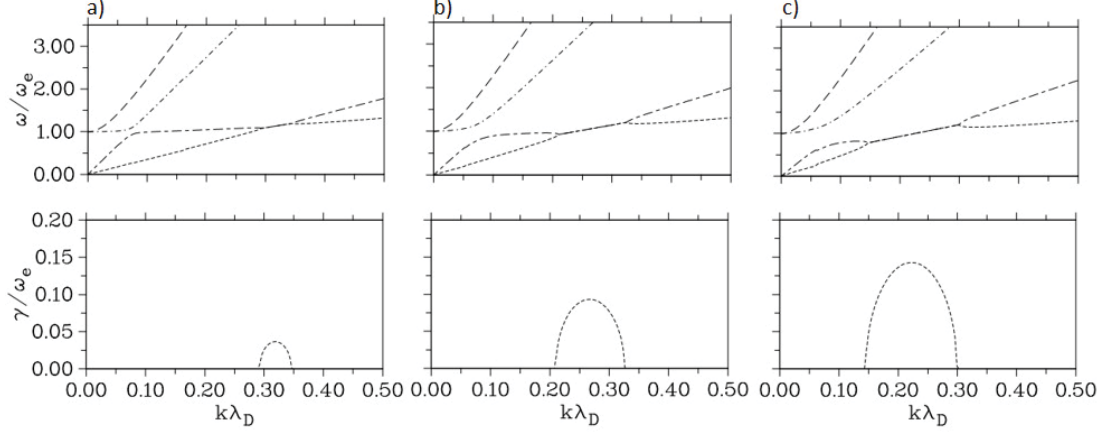


Figure 3.5: Showing the change of wave modes and maximum growth rate of the beam instability with the change of main to beam electron density ratio,  $\mu = n_{po}/n_{eo}$  where  $\theta = 30^\circ$ ,  $c/V_{Te} = 0.05$ ,  $V_p = 10$ ,  $U_p = 3$ , and (a)  $\mu = 0.01$ , (b)  $\mu = 0.05$ , (c)  $\mu = 0.09$ .

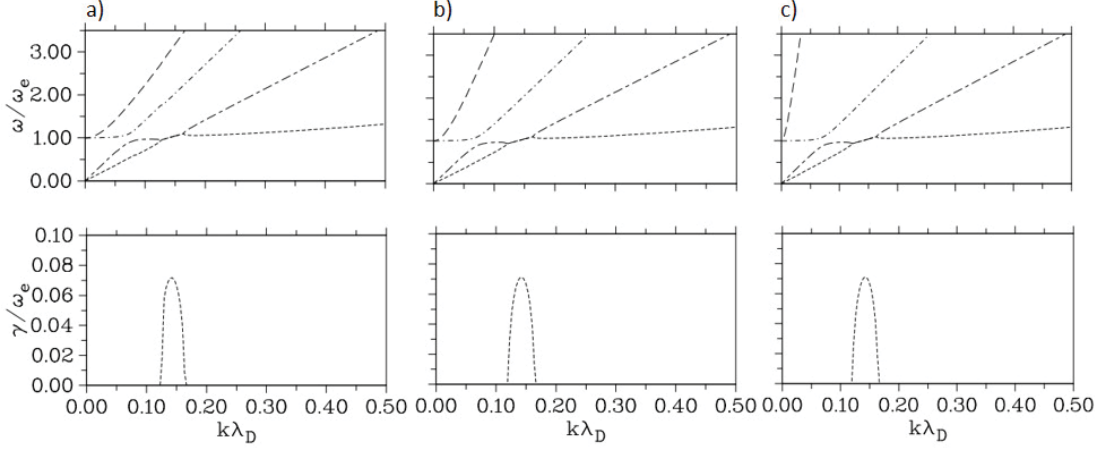


Figure 3.6: Showing the change of wave modes and maximum growth rate of the beam instability with the change of  $c/V_{Te}$  where  $\theta = 30^\circ$ ,  $\mu = 0.01$ ,  $V_p = 12$ ,  $U_p = 3$ , and (a)  $c/V_{Te} = 0.01$ , (b)  $c/V_{Te} = 0.03$ , (c)  $c/V_{Te} = 0.05$ .

figure, it is clear that there is no significant change in the light wave mode with the change of density ratio, but the Langmuir mode shifts slightly towards larger wave number. On the other hand the position of the maximum growth rate changes with the change of the value of  $\mu$ . When  $\mu = 0.01$ , the wavenumber of maximum instability is at  $k\lambda_D \sim 0.35$  as shown in figure 3.5(a). If we increase the value of  $\mu$ , maximum instability becomes broader and shifts towards smaller wavenumber. Also, the height of the maximum instability increases with the increase of the value of  $\mu$  as in figures 3.5(a-c).

Figure 3.6 Shows the change of wave modes and maximum growth rate of the beam instability with the change of the value of  $c/V_{Te}$ . From this figure, we have found that there is no significant change of the Langmuir mode with of the value of  $c/V_{Te}$ , but the light mode shifts towards smaller wave number. Also maximum instability remains constant if we change the value of  $c/V_{Te}$  as shown as figure 3.6(a-c).

## 3.8 Summary

We have considered a simplified beam plasma system consisting of main and beam electrons to investigate the saturation of the beam instability. Electromagnetic fluid model has been considered and the characteristics signature of the transition from beam instability to a saturated state has been described from the solution of the dispersion relation. The results, which have been found in this investigation may be pointed out as follows:

1. When the velocity of the beam electrons is in resonance with the phase velocity the Langmuir waves becomes excited.
2. Saturation occurred when the beam instability is completely quenched as the gap in velocity space between the beam and the main plasma diminishes.
3. Mode splitting, instability, and the saturation of the of the beam plasma significantly changes with the change of the plasma parameters such as beam velocity, thermal velocity, electron density, the angle between the x-axis and the direction of the streaming plasma, etc.
4. When the beam is heated and a lowering of its drift velocity takes place, the maximum growth rate of the beam instability goes down and shifts to larger wave numbers.
5. With the increase of the density ratio, maximum instability increases, becomes broader, and shifts towards smaller wavenumber. Langmuir mode also shifts slightly towards larger wave number.
6. Due to the increase in the value of  $c/V_{Te}$ , the light mode shifts towards smaller wave number, but maximum instability remains constant.

The results found here is similar to the results investigated by Sauer and Sydora for electrostatic case [55]. It should be mentioned here that the general trend of our fluid approach with respect to the beam instability remains nearly the same. The modifications are due to the consideration of the more general electromagnetic plasma fluid model. The results found from this investigation is important as the saturation state acts a driver of the homogeneous electric field oscillations at plasma frequency. We will discuss this further in Chapter 5.

# Chapter 4

## Particle-in-Cell Model

### 4.1 Introduction

Our natural world can be described based on the description of the interacting elements of matter via force fields. Plasma is a good example because it is composed of charged particles such as electrons, ions, and charged dust grains. Plasma particles are interacting via electric and magnetic fields. Particles move due to their own and applied fields. Computer simulations of such a system can be conducted by following each particle in the system and their fields. Simulation continues discontinuously in time step by step which is digital[62]. Therefore, particle models are considered a highly successful model in the simulation of plasmas. However, numerical methods that provide sufficient accuracy and stability should be taken carefully to make the simulations useful. Particle-In-Cell (PIC) method is a computational simulation method which uses macro-particles or super particles to represent the real ions, electrons, and neutrals. Thus a particle represents many particles. PIC codes are useful when differential equations describe fields in terms of particle sources. In PIC simulation, the force acting on the particles are calculated from the fields rather than direct binary interactions which reduces calculation to order  $n$  rather than  $n^2$ [62]. PIC codes are useful in almost all areas of plasma physics, such as plasma accelerators, space physics, fusion energy research, ion propulsion, plasma processing, etc.

## 4.2 Overview of PIC model

Various PIC codes, such as electrostatic, magnetostatic, electromagnetic, etc. are used depending on the kind of forces that are included in the plasma description. In this thesis, we concentrate on the electrostatic and electromagnetic particle in cell codes. However, to simplify our discussion, we first discuss the basics of the electrostatic PIC code. Interaction of charged particles can be described by Coulomb's law as follows

$$\mathbf{F} = \frac{1}{4\pi\epsilon_0} \frac{q_1 q_2}{r^3} \mathbf{r}_{12}, \quad (4.1)$$

where  $q_1$  and  $q_2$  represent the charges of the two particles,  $r$  is the distance between them, and  $\epsilon_0$  is the vacuum permittivity constant. Plasma simulation could be performed by taking all the real physical ions and electrons and directly computing the force using above Coulomb's force equation. Generally, plasma simulations require at least 1 million particles. As Coulomb force leads to an  $n^2$  problem, computation of a single time step would require at least 1 trillion operations which very difficult to perform. Therefore, as we mentioned earlier, super particles are considered and the force acting on charged particles is calculated by using the Lorentz Force,

$$\mathbf{F} = q(\mathbf{E} + \mathbf{v} \times \mathbf{B}), \quad (4.2)$$

where  $q$  is the particle charge,  $\mathbf{E}$  is the electric field,  $\mathbf{v}$  is the particle velocity, and  $\mathbf{B}$  is the magnetic field. The motion of each super-particle is governed by Newton's Second Law of motion and the electric potential given by Poisson's equation. The Particle in Cell method consists of the following iterative steps:

- i. *Compute Charge Density*: Charge density is the number of charge units per unit volume. It is computed by distributing charge of all particles onto the nodes of computational cells and then dividing by the corresponding node volume.
- ii. *Compute the electric potential*: The electric potential is calculated by solving Poisson's equation.

- iii. *Compute the electric field*: Electric field is computed from the gradient of the potential.
- iv. *Move the particles*: Positions and velocities of particles are updated by using Newton's Second Law. Particle motions are integrated through a time step. The Leapfrog method is commonly used in PIC codes as it is fast and numerically stable.
- v. *Boundary conditions*: Boundary conditions are applied to continue the simulation.
- vi. *Output results*: Output from PIC codes such as potential, charge density, electron temperature, velocities and current densities, total kinetic and potential energy of the simulation, etc. need to be saved on simulation state at preset time-steps.
- vii. *Repeat*: The loop repeats until conditions are satisfied.

### 4.3 Electrostatic Plasma Simulation Model

For our study of electrostatic plasma, we use one dimensional Particle-in-Cell (PIC) code developed by V. K. Decyk in the UCLA Particle-in-Cell (UPIC) Framework[63; 64]. In the electrostatic problem, the PIC code solves the particle equations of motion and the force of interaction is determined by solving the Poisson equation. The simulation code is one-dimensional and is useful when inductive electric and magnetic fields are not important. Usually, PIC codes are set up as grid systems with grid spacing  $\Delta x$  and periodic boundary conditions. Particles are able to exist anywhere in the cells. Charge density is accumulated on a grid from the particle co-ordinates. Fields are calculated at the grid points and then interpolated back to the particle positions to determine the forces there. There are three important procedures in the main iteration loop. The first step is the deposit where particle quantity such as charge is accumulated on a grid via interpolation to produce. Secondly, the field solver solves Maxwell's equation or a subset to obtain the electric and/or magnetic fields from the source densities. Once the fields are obtained, the particle forces are found by interpolation from the grid. Newton's second law and the Lorentz force are used to update particle co-ordinates[63; 64]. The main interaction loop can be summarised as follows. The charge density  $\rho$  is calculated on a mesh from the particle position:

$$\rho(\mathbf{x}) = \sum_i q_i S(\mathbf{x} - \mathbf{x}_i), \quad (4.3)$$

where  $q_i$  is the charge and  $x_i$  is the position of the  $i$ -th particle. The function  $S(x)$  is known as the particle shape function. This would be a delta function for point particles, but finite size in simulations are commonly used in computer modeling which suppress numerical heating that arises from not being able to resolve particle density fluctuations smaller than the grid spacing [63]. To calculate the field  $E$ , Poisson's Equation or Ampere's law are solved

$$\frac{\partial}{\partial x} E_x = 4\pi\rho, \quad (4.4)$$

$$\frac{\partial}{\partial t} E_x = 4\pi j, \quad (4.5)$$

where  $j$  is the current density and background magnetic field  $\mathbf{B}_0 = \mathbf{0}$ . Poisson's Equation given in Eq. 4.4 does not have  $k = 0$  mode and hence is not suitable to describe the mechanism of current driven Langmuir oscillations in plasma. Instead of Poisson's Equation, one must use Ampere's law given in Eq. 4.5 which has  $k = 0$  mode and therefore is suitable for describing plasma oscillations. The difference between the simulation results found from Poisson's Equation and Ampere's law will be discussed in next chapter. Newton's Law of motion is used to advance particle co-ordinates

$$m_i \frac{d\mathbf{v}_i}{dt} = q_i \int [\mathbf{E}(\mathbf{x})] S(\mathbf{x} - \mathbf{x}_i) d\mathbf{x}, \quad (4.6)$$

$$\frac{d\mathbf{x}_i}{dt} = \mathbf{v}_i, \quad (4.7)$$

where  $m_i$  is the mass and  $v_i$  is the velocity of the  $i$ -th particle. The discrete equations of motion for the particles are described by using Leapfrog method of time stepping as follows:

$$\mathbf{v}_i(t + \frac{\Delta t}{2}) = \mathbf{v}_i(t - \frac{\Delta t}{2}) + \frac{q_i}{m_i}, \quad (4.8)$$

$$\mathbf{x}_i(t + \Delta t) = \mathbf{x}_i(t) + \mathbf{v}_i(t + \frac{\Delta t}{2})\Delta t \quad (4.9)$$

The codes described here are spectral and solve the electric field using Fourier

transforms.

## 4.4 Electromagnetic Plasma Simulation Model

Electromagnetic plasma model includes both plasma waves and electromagnetic waves and the electromagnetic code includes all the electric and magnetic fields described by Maxwell's equation. The charge density  $\rho$  and the current density  $\mathbf{j}$  are calculated on a mesh using particle positions and velocities[63; 64].

$$\rho(\mathbf{x}) = \sum_i q_i S(\mathbf{x} - \mathbf{x}_i), \quad (4.10)$$

$$\mathbf{j}(\mathbf{x}) = \sum_i q_i \mathbf{v}_i S(\mathbf{x} - \mathbf{x}_i), \quad (4.11)$$

where  $q_i$ ,  $x_i$ , and  $v_i$  are the charge, position, and velocity of the  $i$ -th particle. With the definition of charge and current densities given in Eqs. (4.10-4.11), the equation of continuity is automatically satisfied:

$$\nabla \cdot \mathbf{j} = \sum_i q_i \mathbf{v}_i \cdot \nabla S(\mathbf{x} - \mathbf{x}_i)(t) = -\frac{\partial \rho}{\partial t} \quad (4.12)$$

Electric field  $\mathbf{E}$  and magnetic field  $\mathbf{B}$  are obtained by solving maxwell's equation with fast Fourier transforms for periodic boundary condition.

$$\nabla \times \mathbf{B} = \frac{4\pi}{c} \mathbf{j} + \frac{1}{c} \frac{\partial \mathbf{E}}{\partial t}, \quad (4.13)$$

$$\nabla \times \mathbf{E} = -\frac{1}{c} \frac{\partial \mathbf{B}}{\partial t}, \quad (4.14)$$

$$\nabla \cdot \mathbf{B} = 0, \quad (4.15)$$

$$\nabla \cdot \mathbf{E} = 4\pi\rho, \quad (4.16)$$

Lorentz Forces are used to advance particle co-ordinates

$$m_i \frac{d\mathbf{v}_i}{dt} = q_i \int [\mathbf{E}(\mathbf{x}) + \mathbf{v}_i \cdot \mathbf{B}(\mathbf{x})/c] S(\mathbf{x} - \mathbf{x}_i) d\mathbf{x}, \quad (4.17)$$

$$\frac{d\mathbf{x}_i}{dt} = \mathbf{v}_i, \quad (4.18)$$

In discretizing time for the field equations the magnetic field is advanced half a step using the old electric field and then leap-frog the electric field a whole step using the new magnetic field. Finally advance the magnetic field the remaining half step using the new electric field[63; 64].

$$\mathbf{B}(\mathbf{k}, t - \frac{\Delta t}{2}) = \mathbf{B}(\mathbf{k}, t - \Delta t) - i c \mathbf{k} \times \mathbf{E}(\mathbf{k}, t - \Delta t) \frac{\Delta t}{2}, \quad (4.19)$$

$$\mathbf{E}(\mathbf{k}, t) = \mathbf{E}(\mathbf{k}, t - \Delta t) + [i c \mathbf{k} \times \mathbf{B}(\mathbf{k}, t - \frac{\Delta t}{2}) - 4 \pi \mathbf{j}(\mathbf{k}, t - \frac{\Delta t}{2})] \Delta t, \quad (4.20)$$

$$\mathbf{B}(\mathbf{k}, t) = \mathbf{B}(\mathbf{k}, t - \frac{\Delta t}{2}) - i c \mathbf{k} \times \mathbf{E}(\mathbf{k}, t) \frac{\Delta t}{2}. \quad (4.21)$$

The time step should be short enough to maintain the Courant condition  $c \Delta t \leq \Delta$ . The discrete equations of motion for electromagnetic case are given by

$$\mathbf{v}_i(t + \frac{\Delta t}{2}) = \mathbf{v}_i(t - \frac{\Delta t}{2}) + \frac{q_i}{m_i} [\mathbf{E}(\mathbf{x}_i(t)) \quad (4.22)$$

$$+ \frac{1}{2} (\mathbf{v}_i(t + \frac{\Delta t}{2}) + \mathbf{v}_i(t - \frac{\Delta t}{2})) \times \frac{1}{c} \mathbf{B}(\mathbf{x}_i(t))] \Delta t, \quad (4.23)$$

$$\mathbf{x}_i(t + \Delta t) = \mathbf{x}_i(t) + \mathbf{v}_i(t + \frac{\Delta t}{2}) \Delta t \quad (4.24)$$

## 4.5 Summary

In this chapter, we have discussed the fundamentals of the particle-in-cell code and explained the governing equations for both electrostatic and electromagnetic cases based on the code developed by V. K. Decyk[63; 64]. Electrostatic PIC model is useful when inductive electric and magnetic fields are not important whereas electromagnetic PIC code includes all the electric and magnetic fields described by Maxwell's equation. However, in this thesis, both electrostatic and electromagnetic PIC codes are used to investigate the properties of the Langmuir oscillations in the solar wind. The simulation results for both cases will be discussed in the next chapter.

# Chapter 5

## Beam Plasma Instability Analysis

### 5.1 Introduction

Beam-plasma interaction and Langmuir oscillations have attracted a great deal of interest due to their enormous applications in astrophysics especially to find out the mechanism of the Langmuir amplitude modulations and harmonic waves observed in several spacecraft measurements in the solar wind and in planetary region [47; 55; 56; 65; 66; 67]. In Chapter 3, we have investigated the linear dispersion analysis and found that beam becomes saturated in different plasma conditions. When the beam becomes stable no wave activity is expected, but different theoretical, laboratory, and space observations reveal the opposite scenario i.e., wave activity are found even after the beam is out of resonance with the phase velocity of the waves and the wave number ranges are well separated from maximum linear instability[55; 68; 69; 70; 71].

Common interpretations to explain the wave activity are wave-wave interaction and parametric decay[42]. One of the most effective proposed beam stabilization mechanisms is the strong turbulence processes which can pump the Langmuir waves toward higher wave numbers. It is possible because of very intense Langmuir waves associated with the type III bursts. Oscillating two-stream instability, also known as supersonic modulational instability, is a strong turbulence process and it excites a low-frequency ion density perturbation of a given frequency and wave number. Its beat with beam-excited Langmuir waves of different frequencies and wave numbers produce high-frequency down-shifted and up-shifted sidebands.[44]. Spatial collapse related to modulational instability occurs due to intensification of the localized Langmuir wave packet in the self-generated

shrinking density cavity[50]. As an alternative mechanism, Sauer and Sydora [55] introduced antenna concept and argued that the plateau plasma acts as a driver of wave modes beyond the beam instability.

In this Chapter, we have considered both electrostatic and electromagnetic plasma models and investigated nonlinear effects by current driven oscillations. In section 2, we have described how the current driven Langmuir oscillation occurs in electrostatic plasma by using particle in cell (PIC) code. Generation of the Langmuir wave packets via modulational instability of current-driven Langmuir oscillations are studied in section 3 for the electrostatic case and in section 4 for the electromagnetic case. Finally, a summary of our findings is presented in section 5.

## 5.2 Current Driven Langmuir Oscillations

We start the PIC simulations with a stable plasma-plateau configuration, similar to that in Figure 3.3(c) in chapter 3. Electron plasma consists of the main electrons and plateau electrons are considered. Charge neutrality is preserved by using a fixed position ion background plasma. The main plasma electrons follow Maxwellian distribution functions and plateau which is formed by superposition of multiple shifted Maxwellian distribution functions. Thus two plasma populations form bump-on-tail distributions as shown in Figure 2.2. We calculated the electric field  $E_x$  by using both Poisson equation and Ampere's law and show the difference between them.

We used particle-in-cell (PIC) simulation developed by V. K. Decyk in the UCLA Particle-in-Cell (UPIC) Framework[63; 64]. The mathematical theory related to PIC simulations are presented in Chapter 4. Periodic boundary conditions are used for fields and particles. Simulation parameters taken are: system size  $L = 512\lambda_D$ , grid spacing  $\Delta x = \lambda_D$ , average particle number  $N = 1100$  particles/cell, and time step  $\omega_e \Delta t = 0.05$ , beam to main electrons density ratio  $\alpha = 0.1$ , normalized velocity of beam electrons  $V_p = 4$  and thermal velocity of beam electrons,  $U_p = 0.3$ . The use of a relatively high beam density is used to overcome the thermal and numerical noise level. Plateau current  $j_p \sim \alpha V_p = 0.4$ . In the PIC simulation model, particle positions are distributed within the computational domain and electric potential and field are calculated from the charge

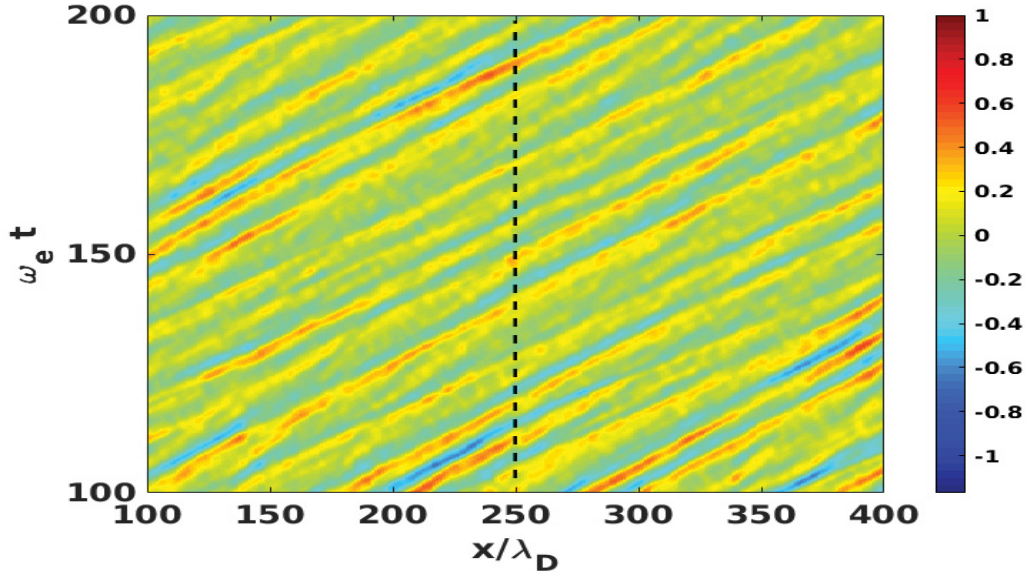


Figure 5.1: The  $x - t$  evolution of the electric field, found from PIC simulation using Poisson equation, exhibits the typical stripe pattern of a propagating wave.

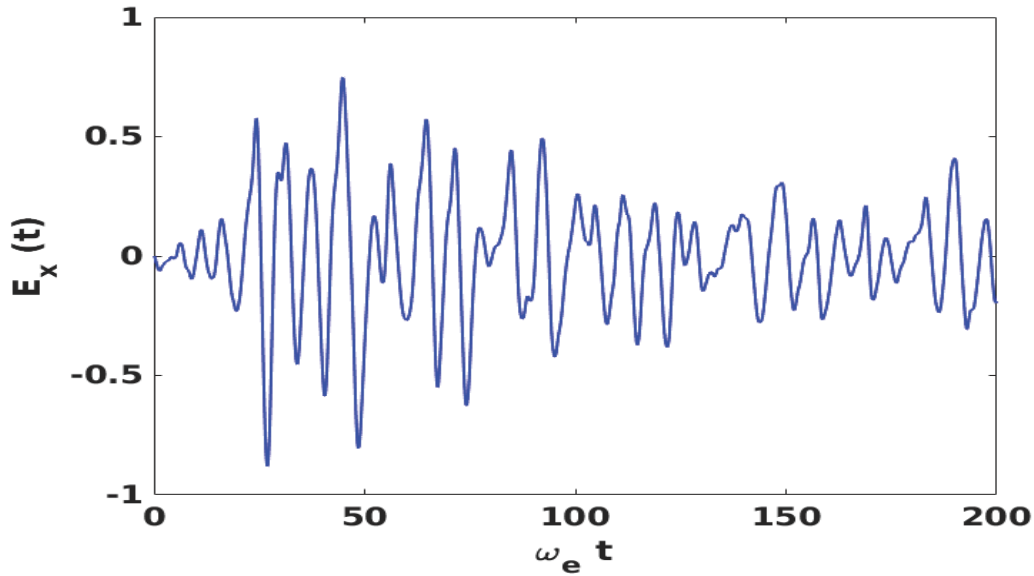


Figure 5.2: Result of PIC simulation using Poisson equation shows the temporal evolution of the electric field at  $x/\lambda_D = 250$ .

density using Ampere's law or Poisson's equation. Positions and velocities of particles are then updated using Newton-Lorentz equation of motion. As we mentioned in the previous chapter, in the Ampere formulation, the  $k = 0$  component describes Langmuir oscillations which are absent in the Poisson formulation.

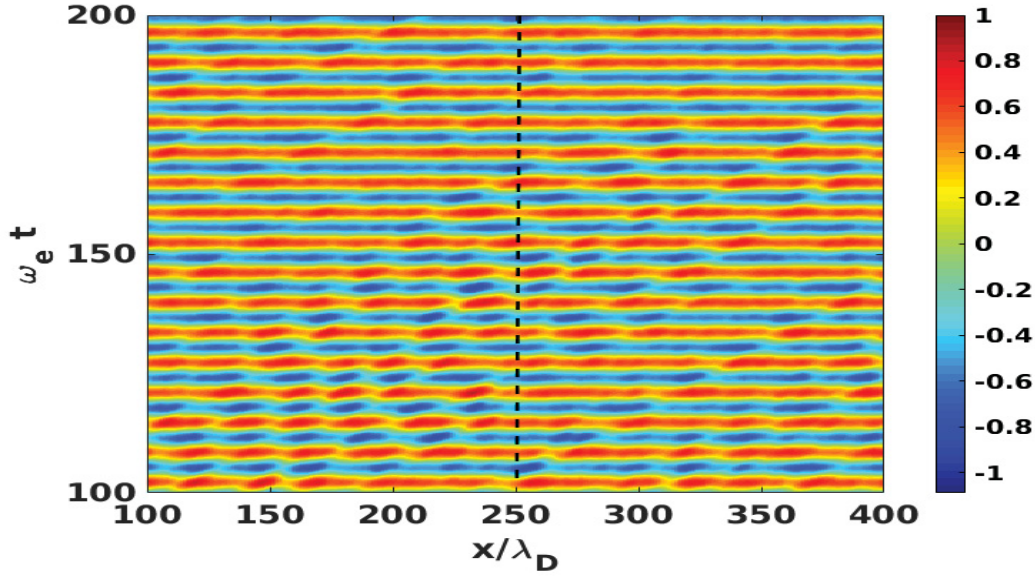


Figure 5.3: The  $x - t$  evolution of the electric field, found from PIC simulation using Ampere's Law, exhibits Langmuir oscillations.

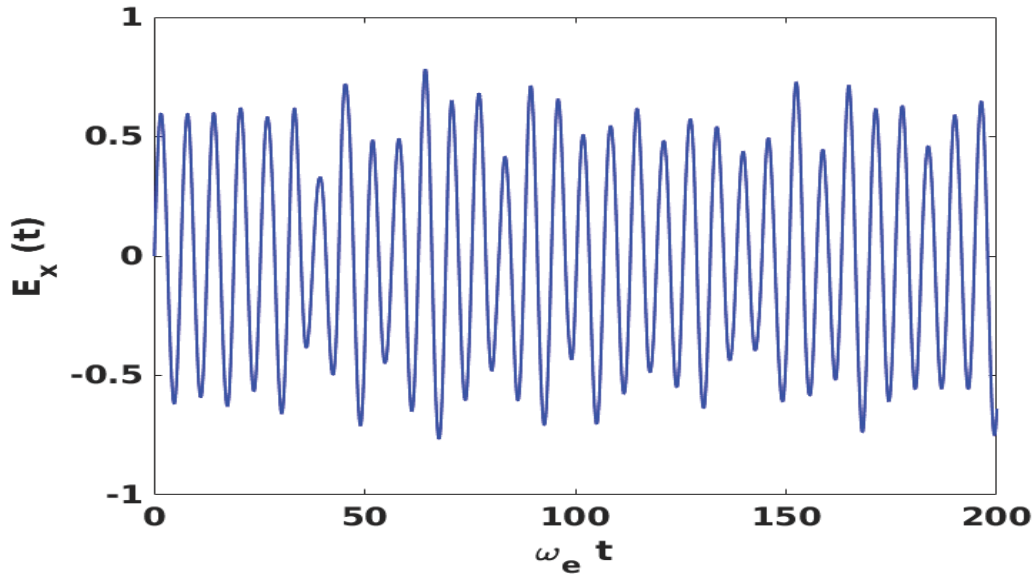


Figure 5.4: Result of PIC simulation using Ampere's Law shows the temporal evolution of the electric field at  $x/\lambda_D = 250$ .

Space-time evolution has been calculated and the simulation results are presented in Figures 5.1-5.4. These Figures demonstrate the different evolution of the electric field according to which equation has been used for its calculation. Figures 5.1-5.2 are found from PIC simulation using Poisson equation. Figure 5.1 shows the  $x - t$  evolution of the electric field and Figure 5.2 shows the periodic variations

of the electric field at  $x/\lambda_D = 250$ . From these Figures, it is clear that Poisson's equation gives the typical stripe pattern of a propagating wave with finite phase velocity.

Figures 5.3-5.4 are found by using Ampere's law. Figure 5.3 shows the  $x - t$  evolution of the electric field. Ampere's law gives the horizontal colored lines exhibiting Langmuir oscillations ( $\omega \sim \omega_e$ ,  $k \sim 0$ ) which is driven by the finite current in the plasma. Figure 5.4 shows the periodic variations of the electric field at  $x/\lambda_D = 250$ . The periodic variations of the electric field are a clear manifestation of current-driven Langmuir oscillations at the plasma frequency  $\omega_e$ . This only occurs if the plasma is described by Ampere's law.

### 5.3 Modulational Instability: Electrostatic Case

The electric field of Langmuir oscillations can act as a pump wave and generate Langmuir envelope solitons as nonlinear effects via modulational instability. Due to its low threshold, the modulational instability can arise spontaneously. To investigate nonlinear effects we used kinetic PIC simulations for the electrostatic case. We consider ions that are not drifting, but electrons have a relative drift motion with  $v_d = 0.2$  against the ions to drive Langmuir waves. Periodic boundary conditions for the fields and particles are used as before. Simulation parameters used are system size  $L = 500\lambda_D$ , grid spacing  $\Delta x = \lambda_D$ , number of grid points = 1024, average particle number  $N = 3000$  particles/cell, ratio of the electron temperature to the ion temperature  $T_e/T_i = 100$ , ion to electron mass ratio  $m_i/m_e = 64$ , and the time step  $\omega_e\Delta t = 0.2$ . We used Ampere's law given in Eq. 4.5 which has  $k = 0$  mode and therefore is suitable for describing plasma oscillations.

Figure 5.5 shows space-time evolution of the electric field amplitude  $E(x, t)/E_0$  for electrostatic case in the time interval  $\omega_e t = 500 - 2500$ . Below  $\omega_e t = 500$  only Langmuir oscillations with random density variations exist. This figure shows that the field structures become visible and solitons are formed. Figure 5.6 shows spatial profile related to Fig. 5.5 at  $\omega_e t = 800$ . From the spatial field in Figure 5.5 one can deduce a wavelength of roughly  $\lambda = 80\lambda_D$  which corresponds to a wave number of  $k\lambda_D \sim 0.08$ . Similar results are found from density profiles shown in Figures 5.8-5.9. Figure 5.8 shows the space-time evolution of the ion density

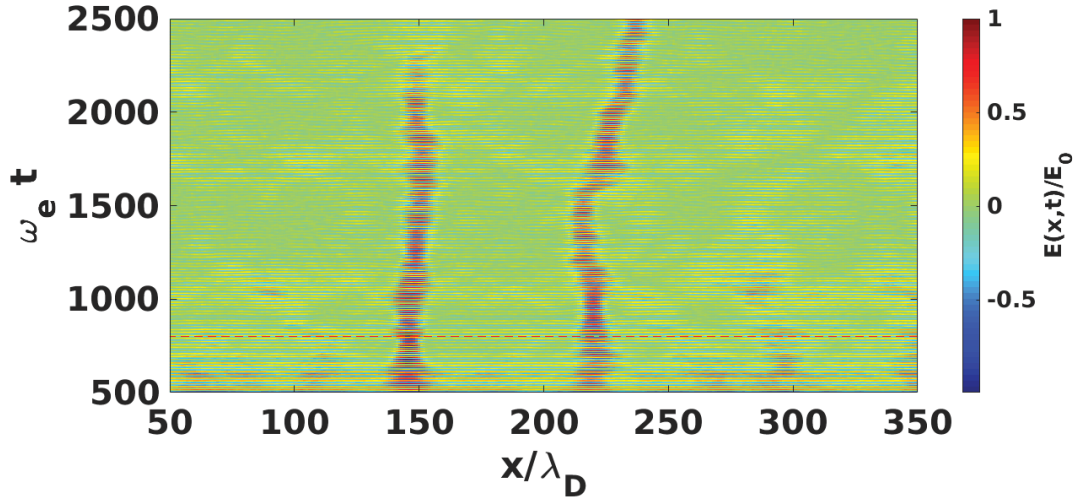


Figure 5.5: Shows the space-time evolution of the electric field amplitude  $E(x,t)/E_0$  where field structuring become visible and solitons are formed due to the modulational instability.

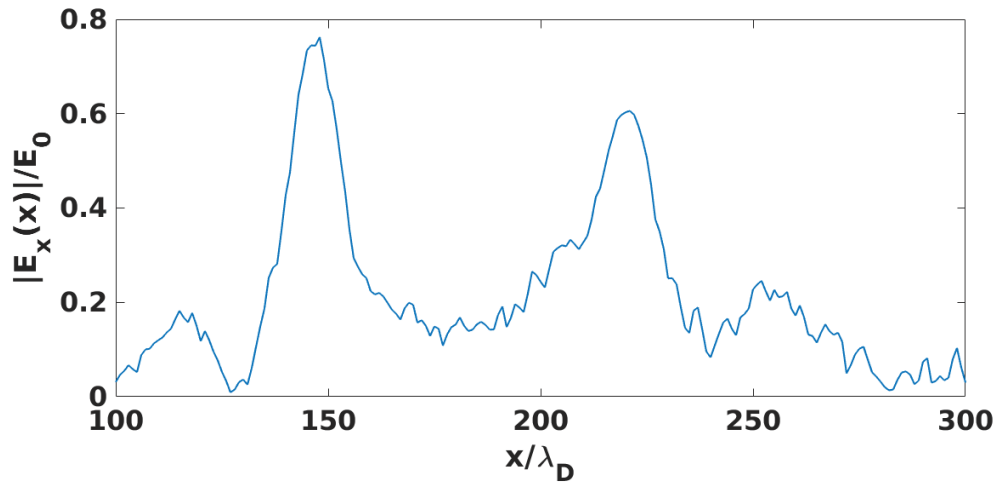


Figure 5.6: Shows spatial profile related to Fig. 5.5 at  $\omega_e t = 800$ .

$n_i(x,t)/n_0$  and Figure 5.9 shows related spatial profile at  $\omega_e t = 800$ . It is clear from these figures that the density structures become visible and cavitons are formed, probably due to the modulational instability. From the spatial profile of ion density wavelength is about  $80\lambda_D$  which is same as the wavelength found from the spatial profile of the electric field. Therefore wave number  $k\lambda_D \sim 0.08$  in both cases.

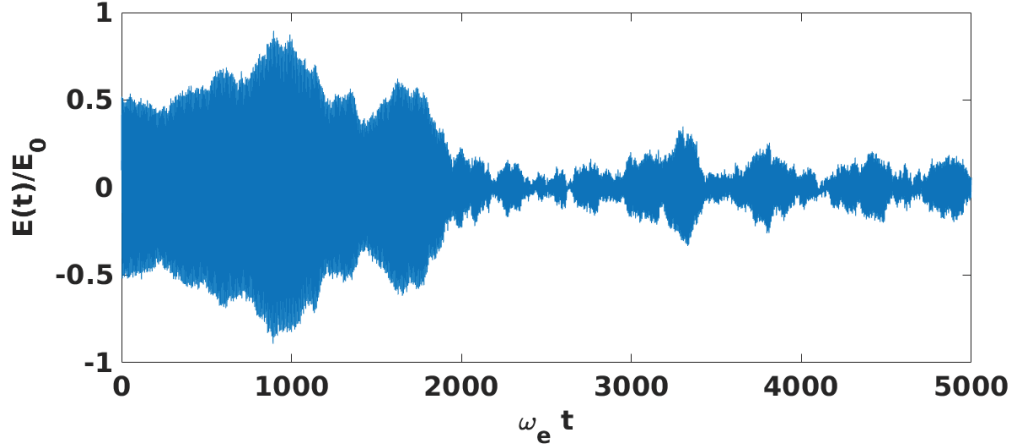


Figure 5.7: Shows temporal variation of of the electric field  $E(t)/E_0$  at  $x/\lambda_D = 220$ .

Figures 5.10 and 5.11 show the power spectrum of the electric field  $E(\omega)$  at  $x/\lambda_D = 220$ . Figure 5.10 shows two well-defined peaks near plasma frequency,  $\omega_e$  whereas figure 5.11 shows double peaks with low frequency near  $\omega = 0.07\omega_e$ . We will discuss them more detail when we compare our result with space observation in Section 5.5.

Now we examine how solitons and cavitons are formed are due to modulational instability. Two electron waves of frequency and wavenumber  $\omega_1, k_1$  and  $\omega_2, k_2$  respectively can beat to form an amplitude envelope travelling at a velocity  $v_g = (\omega_2 - \omega_1)/(k_2 - k_1)$ . This velocity may be low enough to lie within the ion distribution function and there can be an energy exchange with the resonant ions. The ions see the effective potential due to the ponderomotive force and the Landau damping or growth can occur. Damping provides an effective way to heat ions with high frequency waves. If the distribution is double humped it can excite the electron waves and causes modulational instability. When an electron plasma waves go nonlinear, the ponderomotive force of the plasma waves causes the background plasma to move away, causing a local depression in density called a caviton. Plasma waves trapped in this cavity then form an isolated structure called an envelope soliton. solitons are propagating structures maintaining their shape through the balance between nonlinearity and dispersion. The ponderomotive force caused by the envelope of a modulated waves can trap particles and cause wave particle resonance at the group velocity [31].

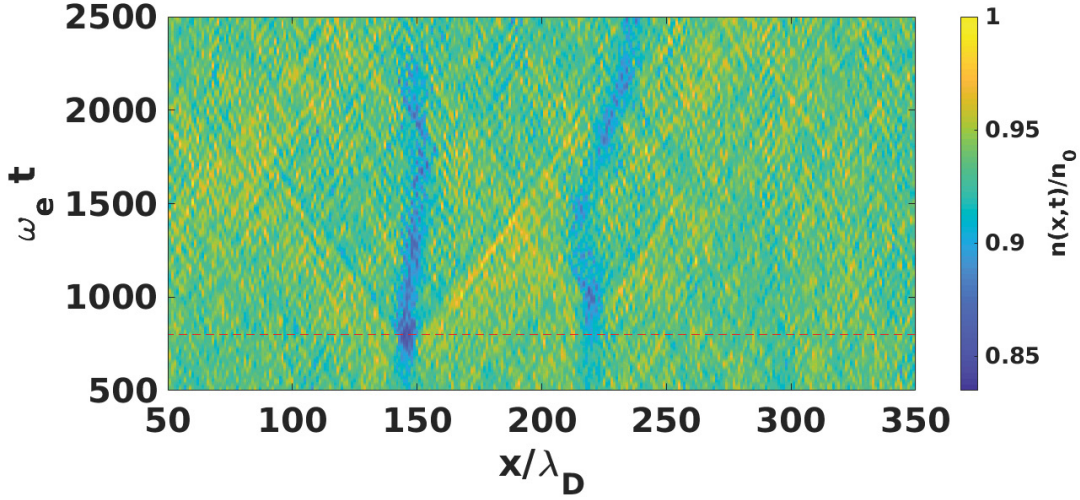


Figure 5.8: Shows the space-time evolution of the ion density  $n_i(x,t)/n_0$ . Density structuring become visible and cavitons are formed due to the modulational instability.

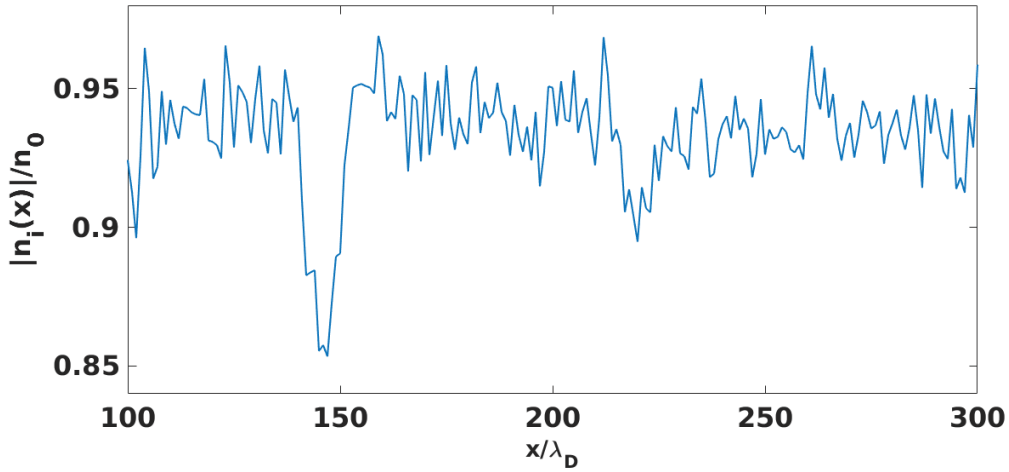


Figure 5.9: Shows spatial profile related to Fig. 5.8 at  $\omega_e t = 800$ .

Modulational instability and soliton-caviton formation in Figures 5.5-5.9 can be explained from the solutions of the Zakharov equation [45]. A solution of the Zhakharov equation for a localized caviton is given by

$$\delta E \propto \frac{1}{L} \operatorname{sech}\left(\frac{x}{L}\right), \quad (5.1)$$

where  $\delta E$  is the change in electric field amplitude or simply  $E/E_0$ .  $E_0$  is the initial electric field amplitude. From the simulation result for spatial field and density

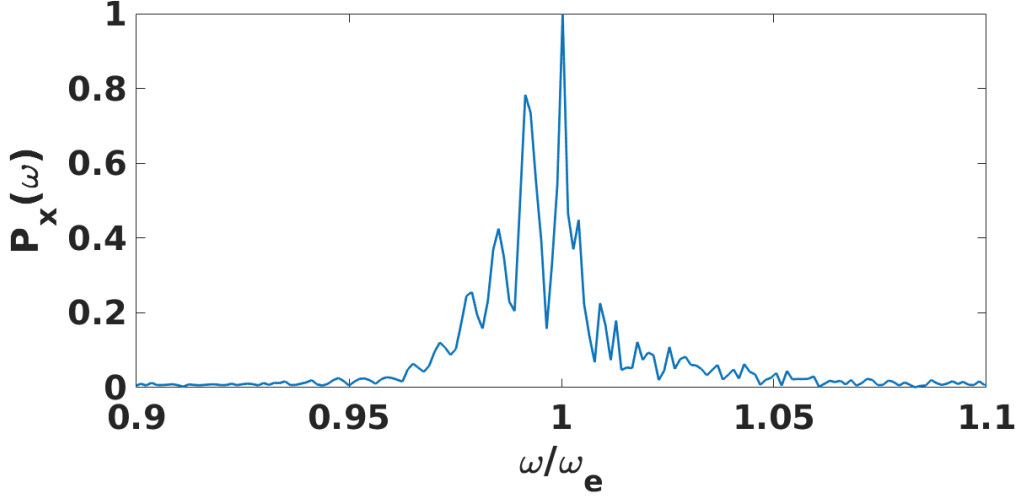


Figure 5.10: Shows the power spectrum of the electric field  $E(\omega)$  at  $x/\lambda_D = 220$ .

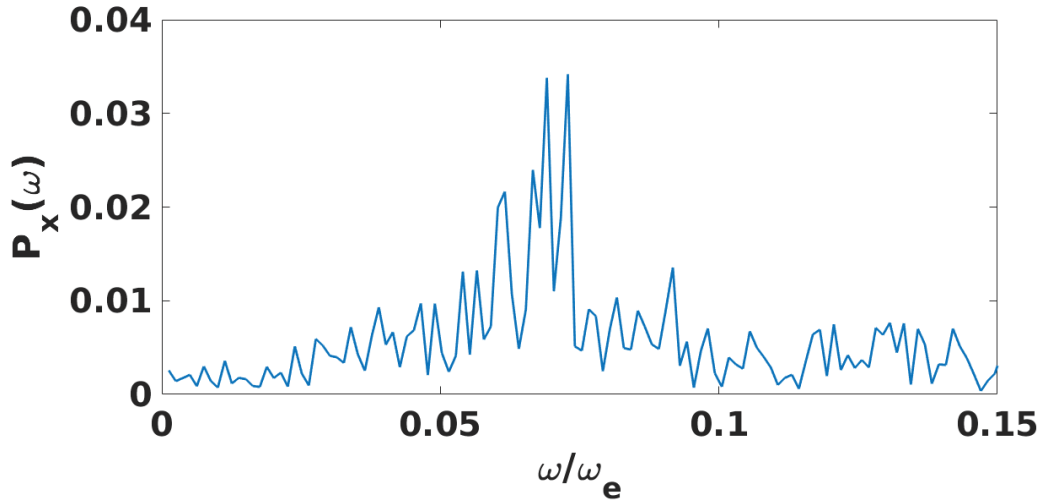


Figure 5.11: Shows low frequency power spectrum of the electric field  $E(\omega)$  at  $x/\lambda_D = 220$ .

profile, the length of the caviton,  $L \sim 80\lambda_D$  which corresponds to a wave number of  $k\lambda_D \sim 0.08$ . Again the Zakharov equation with subsonic approximation predicts ion density depression given by

$$\frac{\delta n_i}{n_0} = \frac{1}{4}|\delta E|^2, \quad (5.2)$$

Figure 5.7 shows the maximum electric field amplitude is about 0.75. Thus  $\delta n_i/n_0 \sim 0.25(E/E_0)^2 \sim 0.14$ . From Figure 5.9 we have found that the value

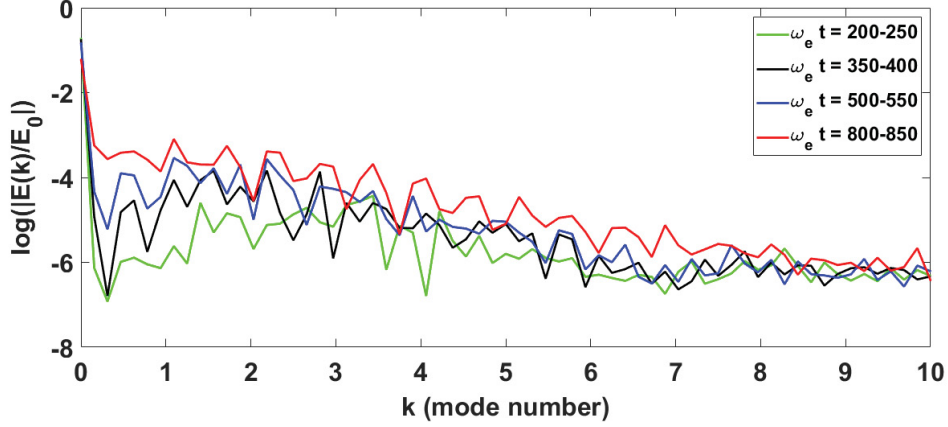


Figure 5.12: Shows how the value of the electric field  $E(k)$  varies with different wave mode number in  $k$ - space for different time ranges.

of  $\delta n_i/n_0$  is around 0.12. Again approximate growth rate can be calculated using the following relation[72]

$$\frac{\gamma}{\omega_e} = \left(\frac{m_e}{3m_i}\right)^{1/2} \frac{E}{2E_0}, \quad (5.3)$$

Theoretically, the growth rate is about  $7 \cdot 10^{-3}$ . From the temporal evolution in Figure 5.7 the roughly estimated growth rate is  $3 \cdot 10^{-4}$  which is close to the theoretical value. Therefore we can say that plasma structuring due to the formation of Langmuir wave packets in Figures 5.5-5.6 are correlated with self-generated ion density depressions shown in Figures 5.8-5.9.

Figure 5.12 shows how the value of the electric field  $E(k)$  varies with different wave mode number in  $k$ - space for different time ranges. The logarithmic values of the average electric field for a particular time ranges ( for example,  $\omega_e t = 350-400$  for black colored plot) are plotted against the wave mode numbers. This figure shows that the value of the average electric field for a particular time range decreases with the increase of the mode number. So, at lower mode number we have high value of the electric field. The wave number  $k$  is defined by

$$k = \frac{2\pi}{\lambda} = \frac{2\pi n}{L}, \quad (5.4)$$

where  $n$  is the mode number and  $L$  is the system length as defined before. There-

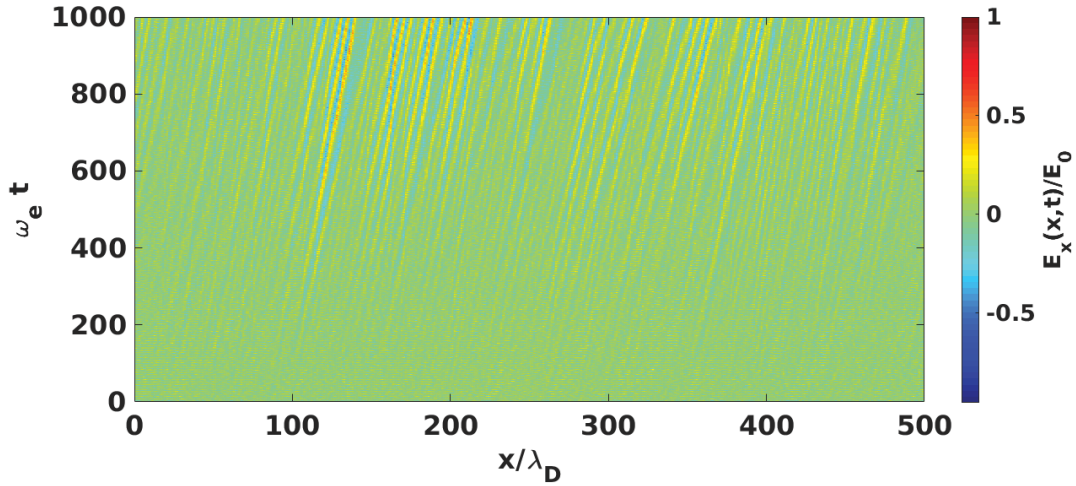


Figure 5.13: Shows the space-time evolution of  $x$ - component of the electric field amplitude  $E_x(x, t)/E_0$  for  $\omega_e t = 0$  to  $\omega_e t = 1000$ .

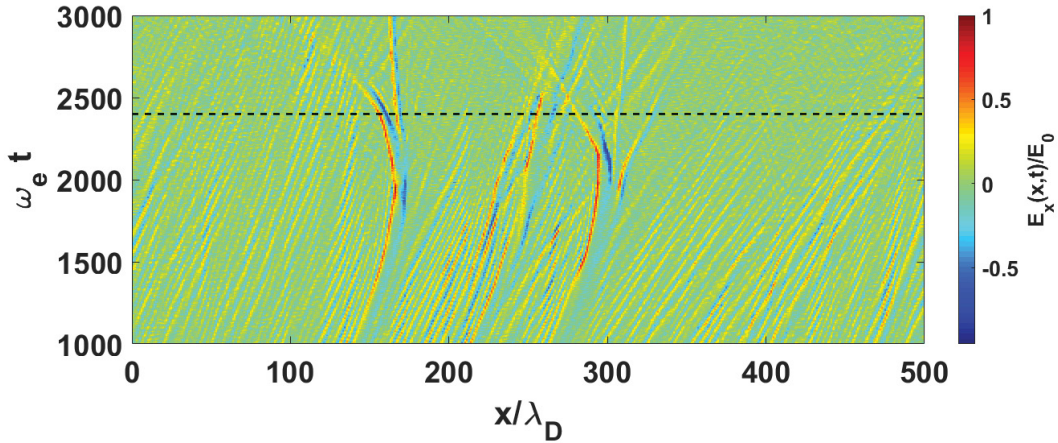


Figure 5.14: Shows the space-time evolution of  $x$ - component of the electric field amplitude  $E_x(x, t)/E_0$  for  $\omega_e t = 1000$  to  $\omega_e t = 3000$ .

fore, for  $n = 1$ , wave number  $k = 2\pi/512 \sim 0.012$ . Therefore, the electric field increase with the decrease of the wave number and reaches maximum with minimum value of the wave number (at  $k = 0$ ). In other word, the electric field is relatively strong at long wavelength. Figure 5.12 also clearly shows the enhancement of the long wavelengths over time.

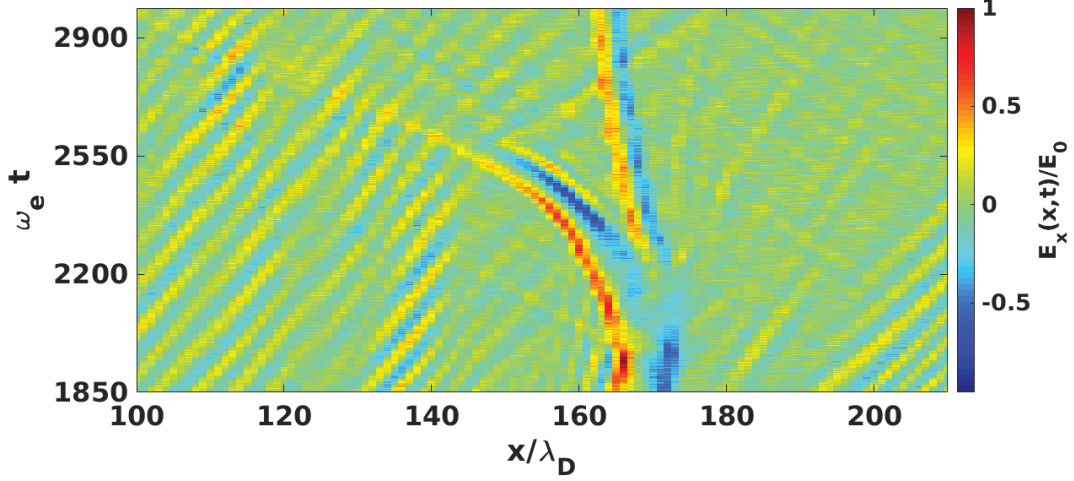


Figure 5.15: Extended view of the space-time evolution of  $x$ - component of the electric field amplitude  $E_x(x, t)/E_0$  for  $\omega_e t = 1850$  to  $\omega_e t = 3000$ .

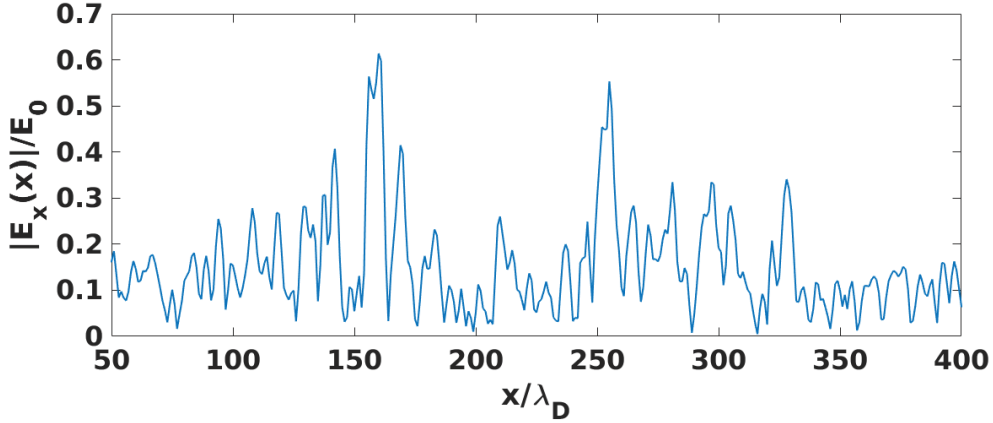


Figure 5.16: Shows spatial profile related to Figure 5.14 at  $\omega_e t = 2400$ .

## 5.4 Modulational Instability: Electromagnetic Case

In this section, we have studied the nonlinear consequence of the current driven Langmuir oscillation for the electromagnetic plasma and investigated the generation and propagation of wave packets. We have found that the electric field of Langmuir oscillations can act as a pump wave and generate Langmuir envelope solitons as nonlinear effects via modulational instability. However, the nature of the evolution of the solitary and density cavity structure in the electromagnetic case is different than the electrostatic case. To investigate nonlinear effects we used kinetic PIC simulations for the electromagnetic case. We consider ions with

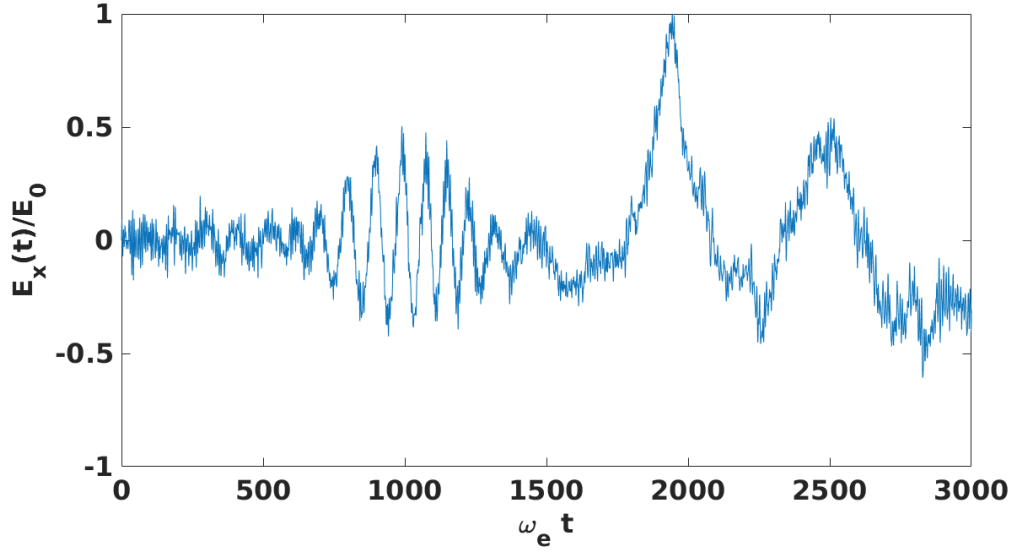


Figure 5.17: Shows temporal variation of  $x$ - component of the electric field  $E_x(t)$  at  $x/\lambda_D = 166$ .

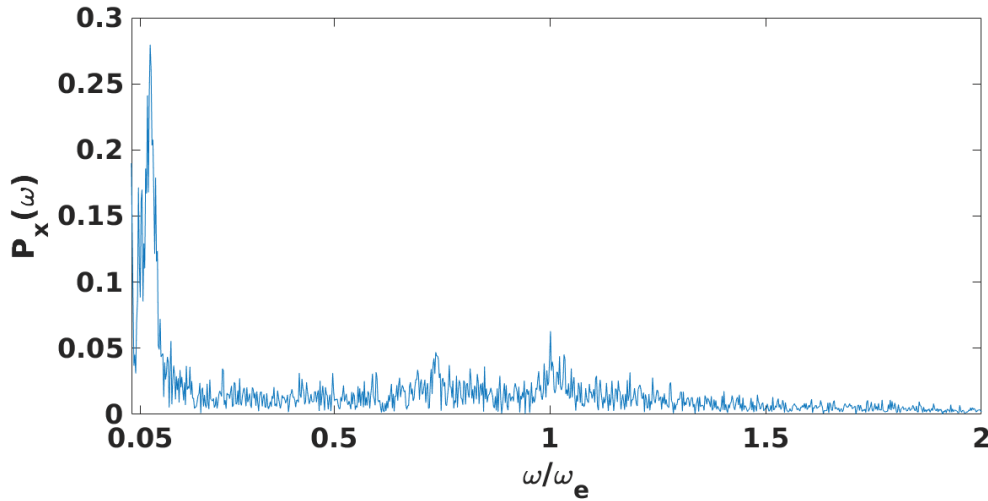


Figure 5.18: Shows power spectrum of  $x$ - component of the electric field  $E_x(\omega)$  for  $x/\lambda_D = 166$ .

no net drift, but electrons have a relative drift motion with  $v_d = 0.3$  against the ions to drive Langmuir waves. Periodic boundary conditions for the fields and particles are used as before. The electromagnetic simulation mode is one-dimensional in space ( $x$ ), three-dimensional in velocity space  $v = (v_x, v_y, v_z)$ , with three-dimensional electromagnetic fields  $E = (E_x, E_y, E_z)$  and  $B = (B_x, B_y, B_z)$ . The wave vector  $k$  is also one-dimensional and lies in the  $x$ - direction. Simulation parameters used are system size  $L = 500\lambda_D$ , grid spacing  $\Delta x = \lambda_D$ , number

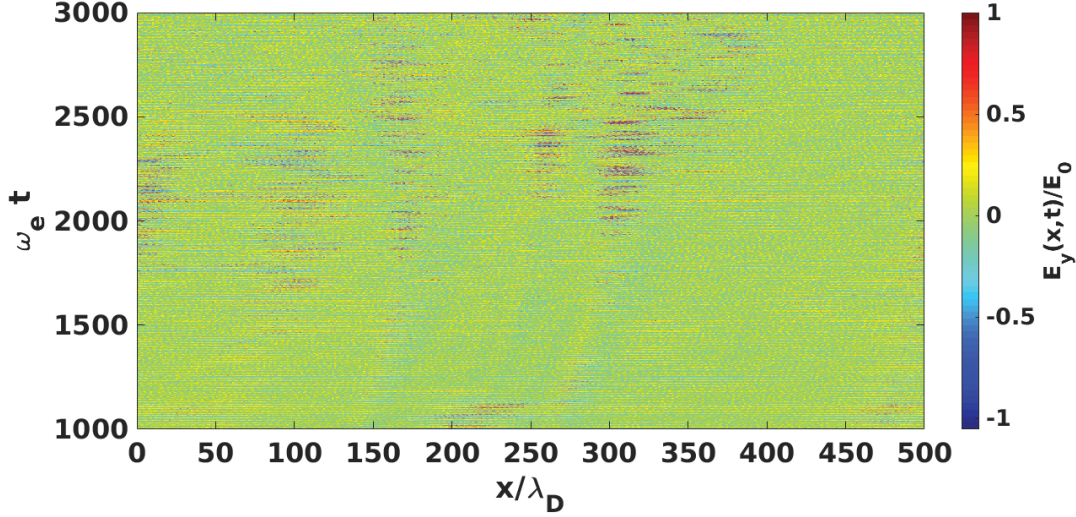


Figure 5.19: Shows the space-time evolution of  $y$ - component of the electric field amplitude  $E_y(x, t)/E_0$ .

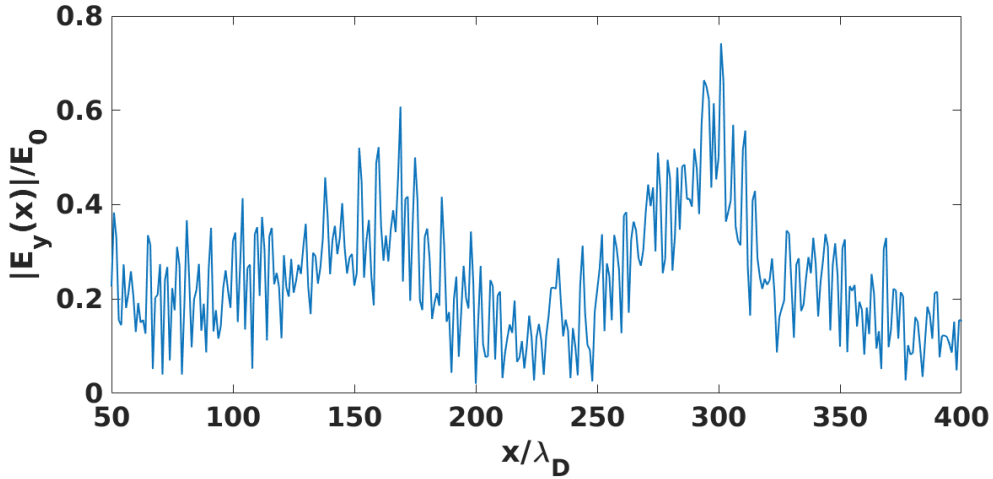


Figure 5.20: Shows spatial profile related to Figure 5.19 at  $\omega_e t = 2200$ .

of grid points = 1024, average particle number  $N = 3000$  particles/cell, ratio of the electron temperature to the ion temperature  $T_e/T_i = 100$ , ion to electron mass ratio  $m_i/m_e = 64$ , normalised velocity of light  $c/V_{Te} = 10$ , and the time step  $\omega_e \Delta t = 0.02$ .

Results found from the electromagnetic PIC simulation are presented in Figures 5.13-5.27. Figure 5.13 shows the space-time evolution of  $x$ - component of the electric field amplitude  $E_x(x, t)/E_0$  for  $\omega_e t = 0$  to  $\omega_e t = 1000$ . From this figure we see that Langmuir oscillations exist, no field structures are formed before  $\omega_e t$

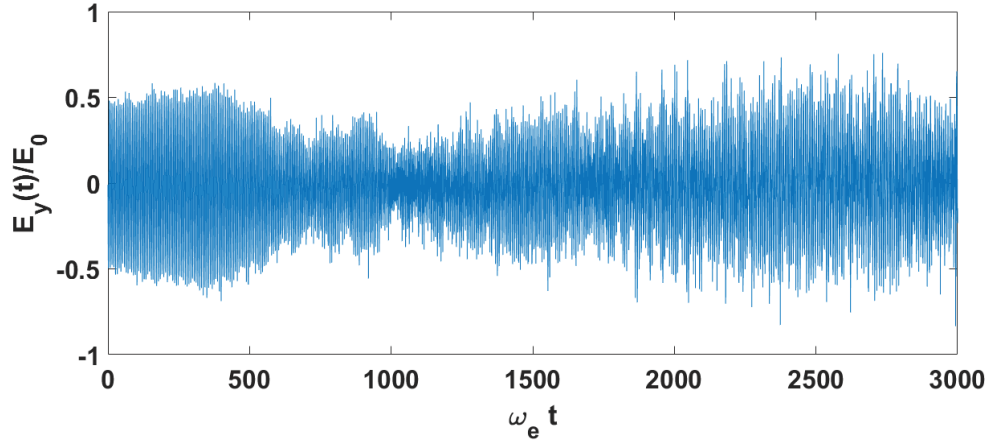


Figure 5.21: Shows temporal variation of  $y$ - component of the electric field  $E_y(t)$  at  $x/\lambda_D = 166$ .

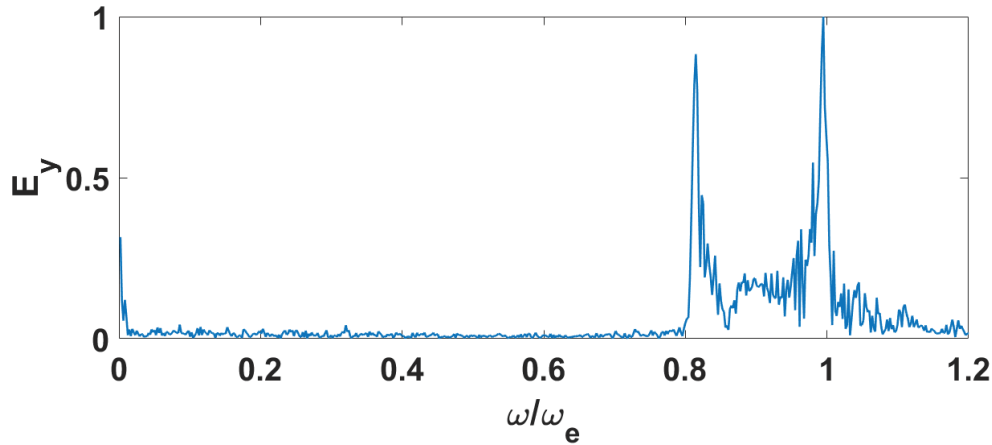


Figure 5.22: Shows power spectrum of  $y$ - component of the electric field  $E_y(\omega)$  for  $x/\lambda_D = 166$ .

$= 500$ . When  $\omega_e t > 500$ , the field structures becomes visible and evolution occurs as shown in Figure 5.14. These solitary structures are formed due to modulational instability as we described in the previous section. Figure 5.15 shows the extended view of the space-time evolution of  $x$  component of the electric field amplitude for  $\omega_e t = 1850$  to  $\omega_e t = 3000$ . From these figures it is clear that the solitary structure remains almost stationary from  $\omega_e t = 1000$  to  $\omega_e t = 1800$ . After  $\omega_e t = 1800$ , it splits into two branches. One branch of wave packets remains stationary and another branch of wave packets start to move (towards left in the figure). The straight red line shows the stationary solitary waves with almost zero phase and group velocity. Thus they are localized in the solar wind. The left

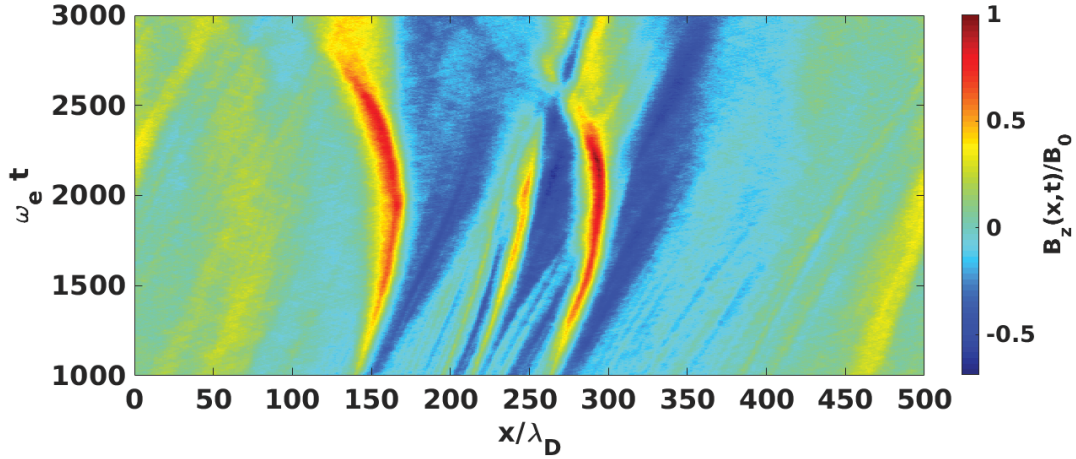


Figure 5.23: Shows the space-time evolution of  $z$ - component of the magnetic field amplitude  $B_z(x,t)/B_0$ .

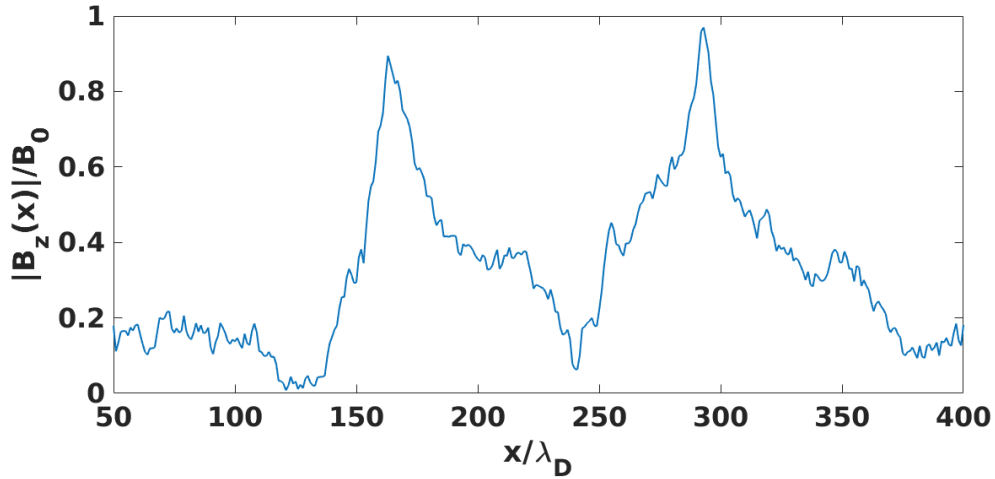


Figure 5.24: Shows spatial profile related to Figure 5.23 at  $\omega_e t = 2200$ .

red curve line shows the propagation of the solitary waves with phase and group velocity.

The spatial profile related to Figure. 5.14 is shown in Figure 5.16 for  $\omega_e t = 2400$ . It shows that the plasma structuring appears at around  $x/\lambda_D = 166$  at  $x/\lambda_D = 255$ . Figure 5.17 shows temporal variation of  $x$  component of the electric field  $E_x(t)$  at  $x/\lambda_D = 166$ . It shows that wave packet forms after  $\omega_e t = 500$ . From  $\omega_e t = 0$  to 1500, the frequency of the oscillations is about  $0.07\omega_e$  which is also clear in power spectrum in Figure 5.18. After  $\omega_e t = 1500$ , it shifts to more lower frequency region (about  $0.0125\omega_e$ ).

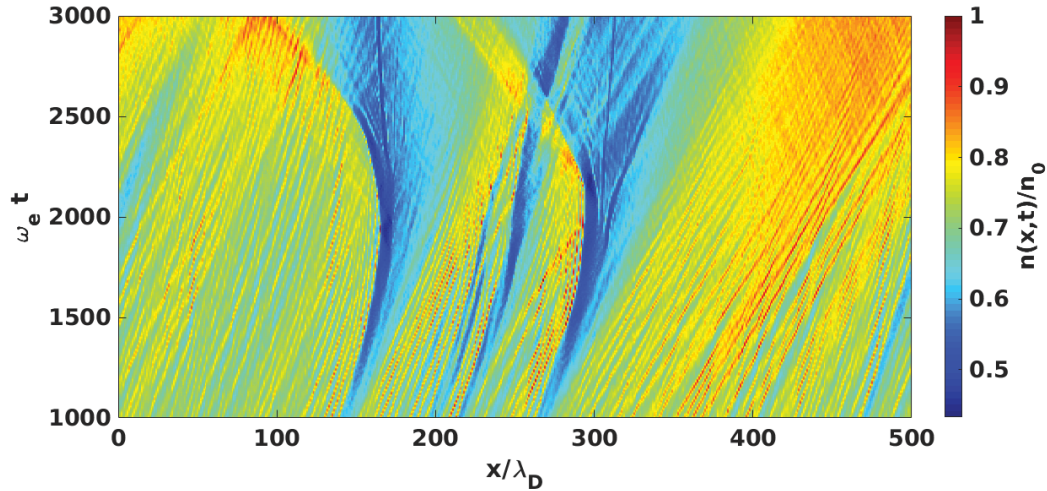


Figure 5.25: Shows the space-time evolution of the ion density  $n_i(x,t)/n_0$  for electromagnetic case.

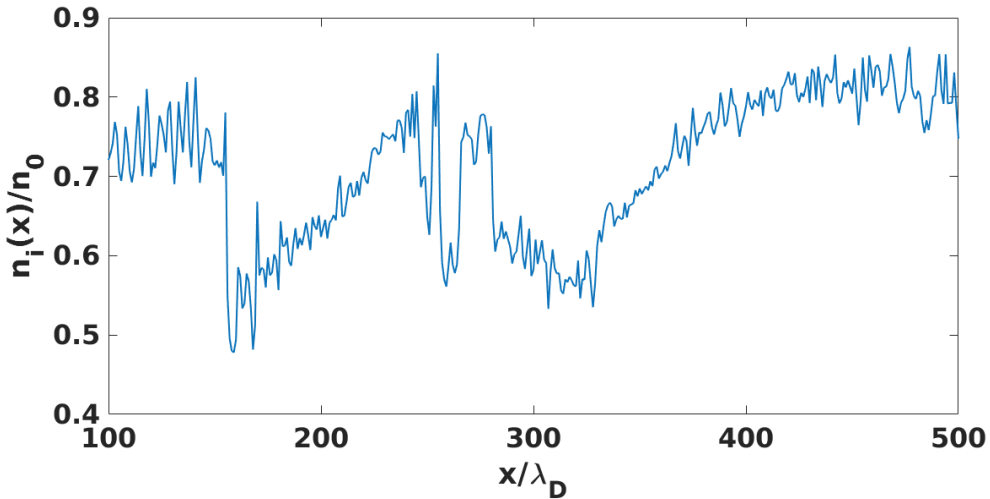


Figure 5.26: Shows spatial profile related to Figure 5.25 at  $\omega_e t = 2400$ .

Now we want to focus on the electromagnetic field components i.e.,  $y$  component of electric field  $E_y$  and  $z$  component of magnetic field  $B_z$ . Figure 5.19 Shows the space-time evolution of  $y$  component of the electric field amplitude  $E_y(x,t)/E_0$ . Spatial profile related to Figure 5.19 at  $\omega_e t = 2200$  is shown in Figure 5.20. It shows that the plasma structuring appears at around  $x/\lambda_D = 166$  at  $x/\lambda_D = 300$ . Temporal variation and power spectrum of  $y$  component of the electric field are presented in Figures 5.21 and 5.22 respectively with  $x/\lambda_D = 166$ . From Figure 5.19 and 5.20, it is clear that solitary structures are formed like in electrostatic

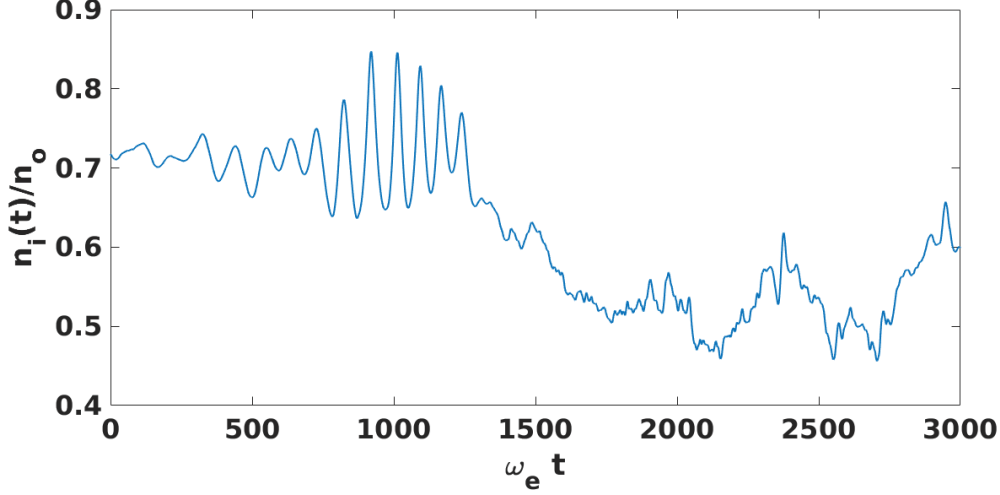


Figure 5.27: Shows temporal variation of the ion density  $n_i(t)$  at  $x/\lambda_D = 166$ .

case, but later their time evolution differs significantly. Power spectrum shows three peaks. One peak is at the plasma frequency  $\omega_e$ , second peak is at  $0.8\omega_e$  and the third peaks is at  $0.002\omega_e$ . Space-time evolution of  $z$  component of the magnetic field amplitude  $B_z(x, t)/B_0$  is shown in Figure 5.23 and their spatial profile is shown in 5.24. Again clear field structuring is visible due to modulational instability. It becomes more clear when we analyze the electromagnetic density profiles given in Figures 5.25-5.27. From space-time evolution of the ion density  $n_i(x, t)/n_0$  in Figure 5.25, it is clear that the density cavities are formed after  $\omega_e t = 500$  and then remains almost stationary from  $\omega_e t = 1000$  to  $\omega_e t = 1800$ . After  $\omega_e t = 1800$ , it splits into two branches. One branch of density cavity remains stationary and other branch starts to move (towards left in the figure). The straight dark blue line shows the stationary density cavity with almost zero phase and group velocity. Thus they are localized in the solar wind. The left blue curve line shows the propagation of density cavity the with finite phase and group velocity.

Figure 5.26 shows the density spatial profile for the electromagnetic case. From the spatial profile of the ion density, the wavelength is about  $100\lambda_D$ . Therefore the wave number  $k\lambda_D \sim 0.06$ . Maximum electric field amplitude is about 0.6. Thus from Eq. 5.3 the maximum field amplitude is correlated with a density depression of about 10%. Figure 5.27 shows the temporal variation of the ion density  $n_i(t)$  at  $x/\lambda_D = 166$ . Figure 5.27 and 5.17 are correlated. Figures 5.20, 5.24 and 5.26 indicate how the electric field and magnetic field amplitude of the

electromagnetic wave and the ion density depression are related. Both  $E_y$  and  $B_z$  fields are at the peak when the density reaches to minimum. This is due to the ponderomotive force of the plasma waves which causes ions to flow towards the minima and the electromagnetic plasma waves trapped in the cavity. It should be noted that for the electromagnetic case soliton-caviton structures are formed like electrostatic case, but later solitary structures delocalize and some energy leaks out from the cavity.

It should be noted here that the normalized peak energy density  $W_L$  controls the nonlinear beam-plasma interaction. If  $W_L \geq (k\lambda_D)^2$ , then the dominant nonlinear beam plasma interactions are the modulational instability and the fully developed soliton formation and collapse[50]. In our study for the electrostatic case,  $k\lambda_D \sim 0.08$  and for the electromagnetic, case  $k\lambda_D \sim 0.06$ . Thus the value of  $(k\lambda_D)^2$  is  $6.4 \cdot 10^{-3}$  and  $3.6 \cdot 10^{-3}$  for the electrostatic and the electromagnetic cases respectively. The energy density  $W_L$  is related to  $E/E_0$  by  $W = (E/E_0)^2/4$ . For the electrostatic case,  $E/E_0 \sim 0.75$  and for the electromagnetic case,  $E/E_0 \sim 0.7$ . Thus  $W_L$  is 0.14 and 0.12 for the electrostatic and the electromagnetic case respectively. Therefore, the conditions are satisfied for the modulational instability in both cases.

## 5.5 Connection to the Space Observation

Numerous publications on spacecraft measurements of wave packet generation and spatial collapse of the Langmuir waves can be found in the literature[34; 49; 50; 51; 52; 53; 54; 67]. There is a broad range of variation of the electric field amplitude from mV/m to V/m in these events. Some events exhibit distinct double peaks near the plasma frequency ( $\sim 30kHz$ ) and many of them have low and high frequency in the power spectrum. In this section, we will discuss two spacecraft events to connect our present study with the observation.

High time resolution observations of a Langmuir wave packet associated with a type III radio burst was investigated by Thejappa et al.[34; 50]. In Chapter 2, Figures 2.1 shows the dynamic spectrum of a local type III radio burst and associated Langmuir waves (non-drifting emissions in the frequency interval 27-32 kHz) of the event observed by STEREO A on 12 September 2010. Related power spectrum is presented in figure 2.3. The power spectrum figure shows the narrow

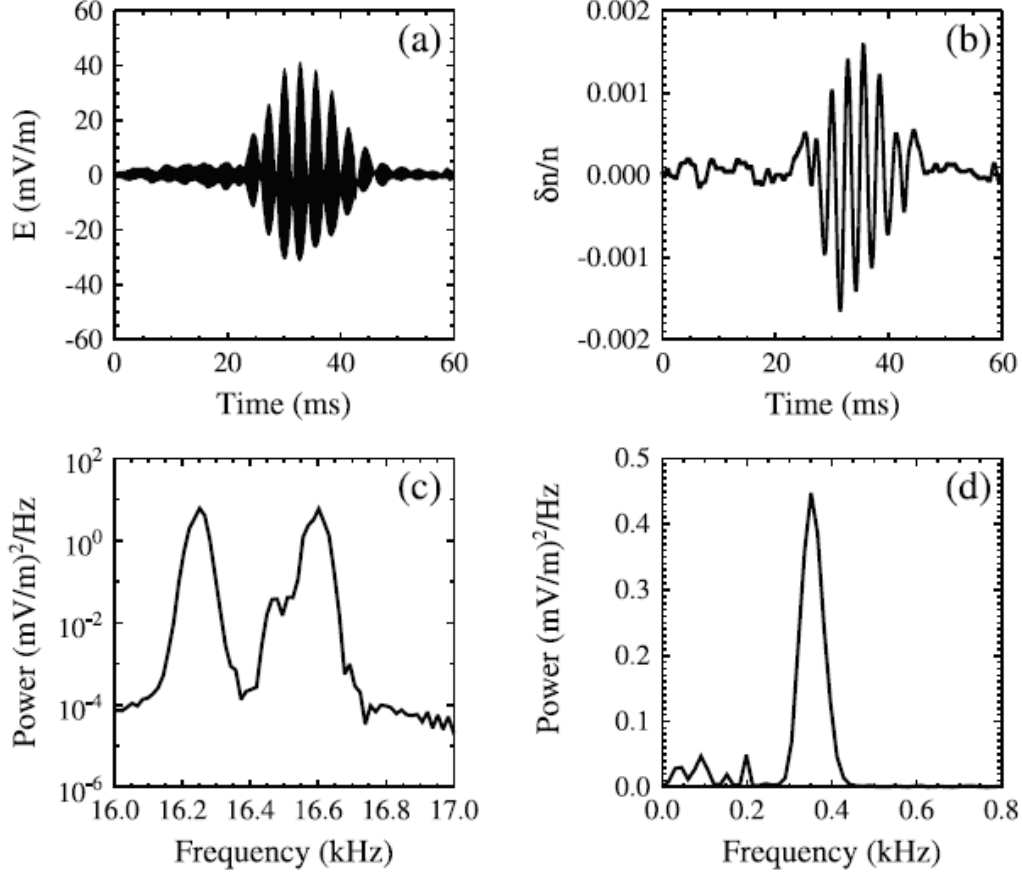


Figure 5.28: Waveform and spectrum of Langmuir waves and density perturbations of the event observed by STEREO A on 19 December 2011 at 13:50:55.160 UT. (a) Waveform of electric field. (b) Density perturbations. (c) Power spectrum near plasma frequency. (d) Power spectrum at low frequency [67].

spectrum containing an intense peak near plasma frequency 30 kHz. The low frequency spectrum was found below 450 Hz. These observations are comparable with our results for both electrostatic and electromagnetic cases. Power spectrum of the electrostatic case as shown in figures 5.10 and 5.11 clearly reveals intense peaks near plasma frequency  $\omega = \omega_e$  and low frequency spectrum near  $\omega = 0.07\omega_e$ . In this case, we have distinct double peaks near the plasma frequency ( $\sim 30\text{kHz}$ ) and at the low frequency region. Power spectrum of  $x$ - and  $y$ - component of the electric field presented in Figures 5.18 and 5.22 respectively shows the similar results found by Thejappa et al. [34; 50]. The low frequency spectrum showing an enhancement below 100 Hz corresponding probably to ion-acoustic waves.

Observation of the STEREO A on 19 December 2011 at 13:50:55.160 UT investigated by Graham and Cairns [67] is shown in Figure 5.28. Figure 5.28(c) and 5.28(d) shows the similar results as we discussed before. Figure 5.28(a) shows the waveform of the Langmuir waves which is comparable with the field oscillation shown in Figure 5.17. Both the observation and simulation show the formation of the Langmuir wave packet. The observed power duration is about 20 ms Graham and Cairns [67] and 3.2ms by Thejappa et al.[34; 50]. From Figure 5.17, we find the duration is about 3ms. As duration can vary from burst to burst, we can say that our simulation results give a reasonable value. Figure 5.28(b) shows that the density perturbations of the event. Comparing Figures 5.28(a) and 5.28(b) with Figures 5.17 and 5.27, we can say that the density perturbations are maximal where the Langmuir waves are most intense. Therefore results from our simulation are qualitatively comparable with the space observations.

## 5.6 Summary

In this Chapter, we have considered electrostatic and electromagnetic plasma models and investigated the mechanism of generation of Langmuir oscillations and their nonlinear effects by using particle in cell (PIC) code. The results, which have been found in this investigation can be summarised as follows:

- i. Saturation process of the beam instability is accompanied by the formation of a plateau distribution and the saturation state represents a current
- ii. Ampere formulation has  $k = 0$  component which is absent in the Poisson's equation. To describe Langmuir oscillations Ampere's law is needed instead of Poisson's equation.
- iii. Current in the saturated state can drive homogeneous electric field oscillations at the plasma frequency.
- iv. Langmuir oscillations ( $\omega = \omega_e, k = 0$ ) act as a specific pump wave for the modulational instability for both electrostatic and electromagnetic cases.
- v. Wave number, maximum amplitude and growth rate conditions for the modulational instability are satisfied in electrostatic and electromagnetic cases.

- vi. In electromagnetic case, solitary structures are formed via modulational instability but later time evolution differs from electrostatic case and the solitary structures become de-localized.
- vii. Density cavities are formed in both electrostatic and electromagnetic cases, but some energy leaks out and comparatively complex structures are formed in the electromagnetic case.
- viii. Simulation results are qualitatively comparable with the spacecraft observations of the Langmuir waves.

# Chapter 6

## Summary and Future Work

In this Chapter, we summarise the main features of this thesis and outline possible future works related to our study.

In Chapter 1, we introduced fundamentals of the solar wind and basic plasma parameters. We discussed the formation, basic properties and space observation of different kinds of solar radio bursts. Fundamentals of plasma physics e.g., Debye shielding, Debye length, plasma frequency, plasma waves, and instability were discussed as they are important for understanding our present study. In Chapter 2, we discussed objective, motivation, and approach of our research. Our primary objective was to study the problem of generation of electromagnetic radiation by solar wind at the plasma frequency and to understand how the continuous type III radiation survives over large distances, e.g., from Sun to Earth.

In Chapter 3, we considered a simplified beam-plasma system consisting of main and beam electrons and investigated the saturation of the beam instability. An electromagnetic fluid model was considered and the characteristics signature of the transition from beam instability to a saturated state had been described from the solution of the dispersion relation. We found that when the velocity of the beam electrons is in resonance with the phase velocity the Langmuir waves becomes excited and saturation occurred when the beam instability is completely quenched, as the gap in velocity space between the beam and the main plasma diminishes. Mode splitting, instability, and the saturation of the of the beam plasma significantly changes with the change of the plasma parameters such as beam velocity, thermal velocity, electron density, angle between the x-axis and the direction of the streaming plasma, etc. When the beam is heated and a

lowering of its drift velocity takes place, the maximum growth rate of the beam instability goes down and shifts to larger wave numbers. With the increase of the density ratio, maximum instability increases, becomes broader, and shifts towards smaller wavenumber. The Langmuir mode also shifts slightly towards larger wave number.

Chapter 4 is the discussion of electrostatic and electromagnetic particle-in-cell (PIC) models which are then used to study kinetic electromagnetic simulations for nonlinear electrostatic and electromagnetic process in Chapter 5. To describe Langmuir oscillations Ampere's law was used instead of Poisson's equation as Ampere formulation has  $k = 0$  component which is absent in the Poisson's equation. We found that the current in the saturated state can drive homogeneous electric field oscillations at the plasma frequency and the electric field of Langmuir oscillations can act as a pump wave and generate Langmuir envelope solitons as a nonlinear effect via modulational instability. We discussed how the wave number, maximum amplitude and growth rate conditions for the modulational instability are satisfied for both electrostatic and electromagnetic cases. We concluded that in the electromagnetic case, solitary structures are formed via modulational instability but later time evolution differs from the electrostatic case and the solitary structure becomes de-localized. The density cavities are formed but some energy leaks out. Finally, simulation results were compared qualitatively with the spacecraft observations.

This work could be extended to include a more detailed analysis of the trapped electromagnetic radiation with density profile. The occurrence of multi-peaked frequency spectra in electromagnetic second harmonic in the form of type III radiation can be analyzed in more detail. Further investigations are needed to study the electromagnetic harmonic generation in space. Theoretical results can be examined more detailed with space observation e.g., TDS events presented by Thejappa et al. [34; 50; 51]. Related proposed mechanisms such as electrostatic decay, electromagnetic decay, nonlinear currents, antenna radiation, and electron trapping can also be compared with our findings, but it beyond the scope of this thesis.

# Bibliography

- [1] W. Baumjohann and R. A. Treumann. *Basic Space Plasma Physics*. Imperial College Press, London, 2012.
- [2] E. Priest. *Magnetohydrodynamics of the Sun*. Cambridge University Press, Cambridge, 2014.
- [3] S. M. White. Solar radio bursts and space weather. *Asian J. Phys.*, 16:189, 2007.
- [4] G. A. Dulk. Radio emission from the sun and stars. *ARA&A*, 23:169, 1985.
- [5] I. H. Cairns *et al.* *Type II Solar Radio Bursts: Theory and Space Weather Implications*. Springer, Dordrecht, 2003.
- [6] H. A. S. Reid and H. Ratcliffe. A review of solar type III radio bursts. *RAA*, 14(7):773, 2014.
- [7] A. O. Benz *et al.* Radio blips and hard X-rays in solar flares. *ApJ*, 271:355, 1983.
- [8] J. L. Melendez *et al.* Statistical analysis of high-frequency decimetric type III bursts. *Sol. Phys.*, 187:77, 1999.
- [9] Y. Leblanc *et al.* The low radio frequency limit of solar type III bursts: Ulysses observations in and out of the ecliptic. *Geophys. Res. Lett.*, 22:3429, 1995.
- [10] Y. Leblanc *et al.* Type III radio bursts observed by ulysses pole to pole, and simultaneously by wind. *A&A*, 316:406, 1996.
- [11] L. G. Evans *et al.* Characteristics of type III exciters derived from low frequency radio observations. *Sol. Phys.*, 31:501, 1973.

## BIBLIOGRAPHY

- [12] H. Alvarez and F. T. Haddock. Decay time of type III solar bursts observed at kilometric wavelengths. *Sol. Phys.*, 30:175, 1973.
- [13] H. Alvarez and F. T. Haddock. Solar wind density model from km-wave type III bursts. *Sol. Phys.*, 29:177, 1973.
- [14] M. Poquerusse. Relativistic type III solar radio bursts. *A&A*, 286:611, 1994.
- [15] A. Klassen *et al.* Superluminal apparent velocities of relativistic electron beams in the solar corona. *A&A*, 410:307, 2003.
- [16] M. J. Aschwanden *et al.* Solar electron beams detected in hard X-rays and radio waves. *ApJ*, 455:347, 1995.
- [17] Y. Ma *et al.* A statistical analysis of the type III bursts in centimeter and decimeter wavebands. *Chinese Astron. Astrophys.*, 36:175, 2012.
- [18] R. R. Weber. Low frequency spectra of type III solar radio bursts. *Sol. Phys.*, 59:377, 1978.
- [19] G. A. Dulk *et al.* Electron beams and radio waves of solar type III bursts. *J. Geophys. Res.*, 103:17223, 1998.
- [20] G. A. Dulk *et al.* Calibration of low-frequency radio telescopes using the galactic background radiation. *A&A*, 365:294, 2001.
- [21] P. Saint-Hilaire *et al.* A decade of solar type III radio bursts observed by the nanÇay radioheliograph 1998-2008. *ApJ*, 762:60, 2013.
- [22] G. A. Dulk and S. Suzuki. The position and polarization of type III solar bursts. *A&A*, 88:203, 1980.
- [23] J. L. Steinberg *et al.* Evidence of scattering effects on the sizes of interplanetary type III radio bursts. *A&A*, 150:205, 1985.
- [24] R. P. Lin *et al.* Simultaneous observations of fast solar electrons and type III radio burst emission near 1 AU. *Astrophys. Lett.*, 14:191, 1973.
- [25] S. Suzuki and G. A. Dulk. *Solar Radiophysics: Studies of Emission from the Sun at Metre Wavelengths*. Cambridge University Press, Cambridge and New York, 1985.

## BIBLIOGRAPHY

- [26] J. P. Wild *et al.* Harmonics in the spectra of solar radio disturbances. *Australian Journal of Physics*, 7:429, 1954.
- [27] R. T. Stewart. Harmonic ratios of inverted-u type III bursts. *Sol. Phys.*, 39:451, 1974.
- [28] P. A. Robinson and I. H. Cairns. Fundamental and harmonic emission in type III solar radio bursts – I. emission at a single location or frequency. *Sol. Phys.*, 181:363, 1998.
- [29] P. A. Robinson and A. O. Benz. Bidirectional type III solar radio bursts. *Sol. Phys.*, 194:345, 2000.
- [30] B. Ghosh. *Basic Plasma Physics*. Alpha Science International Ltd, Oxford, UK, 2014.
- [31] F. F. Chen. *Introduction to Plasma Physics and Controlled Fusion*. Plenum Press, New York, 1984.
- [32] P. K. Shukla and A. A. Mamun. *Introduction to Dusty Plasma Physics*. Institute of Physics Publishing, Bristol, 2002.
- [33] A. G. Emslie *et al.* Global energetics of thirty-eight large solar eruptive events. *ApJ*, 759:71, 2012.
- [34] D. Thejappa *et al.* Phase coupling in langmuir wave packets: Evidence of four wave interactions in solar III radio bursts. *Geophys. Res. Lett.*, 39:L05103, 2012.
- [35] Y. Kasaba *et al.* One- and two-dimensional simulations of electron beam instability: generation of electrostatic and electromagnetic  $2f_p$  waves. *J. Geophys. Res.*, 106:18693, 2001.
- [36] V. L. Ginzburg and V. V. Zhelezniakov. On the possible mechanisms of sporadic solar radio emission (radiation in an isotropic plasma). *J. Soviet Ast.*, 2:653, 1958.
- [37] R. P. Lin *et al.* Energetic electrons and plasma waves associated with a solar type III radio burst. *Astrophys. J.*, 251:364, 1981.
- [38] P. A. Sturrock. AAS-NASA symposium on the physics of solar flares. *NASA-SP*, 50:237, 1964.

## BIBLIOGRAPHY

- [39] D. F. Smith and D. Sime. Origin of plasma-wave clumping in type III solar radio burst sources. *Astrophys. J.*, 233:998, 1979.
- [40] P. A. Robinson and H. I. Cairns. Stochastic growth theory of type III solar radio emission. *Astrophys. J.*, 518:506, 1993.
- [41] S. A. Kaplan and V. N. Tsytovich. Radio emission from beams of fast particles under cosmic conditions. *Sov. Astron. AJ*, 11:956, 1968.
- [42] R.P. Lin *et al.* Evidence for nonlinear wave-wave interactions in solar type III radio bursts. *Astrophys. J.*, 308:954, 1986.
- [43] D. Thejappa *et al.* Evidence for electrostatic decay in the solar wind at 5.2 AU. *Geophys. Res.*, 108:1139, 2003.
- [44] K. Papadopoulos *et al.* Stabilization of electron streams in type III solar radio bursts. *Astrophys. J.*, 190:175, 1974.
- [45] V. E. Zakharov *et al.* Collapse of langmuir waves. *Sov. Phys.-JETP*, 35:908, 1972.
- [46] G. J. Morales and Y. C. Lee. Effect of localized electric fields on the evolution of the velocity distribution function. *Phys. Rev. Lett.*, 33:1534, 1974.
- [47] D. A. Gurnett *et al.* Parametric interaction and spatial collapse of beam-driven langmuir waves in the solar wind. *J. Geophys. Res.*, 86:8833, 1981.
- [48] D. Malaspina *et al.* The  $2f_p$  radiation from localized langmuir waves. *J. Geophys. Res.*, 115:A01101, 2010.
- [49] D. Thejappa *et al.* Evidence for langmuir envelope solitons in solar type III burst source regions. *J. Geophys. Res.*, 104:28279, 1999.
- [50] D. Thejappa *et al.* Evidence for the oscillating two stream instability and spatial collapse of langmuir waves in a solar type III radio burst. *Astrophys. J. Lett.*, 747:L1, 2012.
- [51] D. Thejappa *et al.* Observational evidence for the collapsing langmuir wave packet in a solar type III radio burst. *J. Geophys. Res. Space Physics*, 118:4039, 2013.
- [52] D. Thejappa *et al.* Observational evidence for the collapsing langmuir wave packet in a solar type III radio burst. *Ann. Geophys.*, 31:1417, 2013.

## BIBLIOGRAPHY

- [53] D. B. Graham *et al.* Evidence against the oscillating two-stream instability and spatial collapse of langmuir waves in solar type III radio bursts. *Astrophys. J. Lett.*, 753:L18, 2012.
- [54] D. B. Graham *et al.* Do langmuir wave packets in the solar wind collapse? *J. Geophys. Res.*, 117:A09107, 2012.
- [55] K. Sauer and R. D. Sydora. Current-driven langmuir oscillations and amplitude modulations—another view on electron beam-plasma interaction. *J. Geophys. Res. Space Physics*, 120:235, 2015.
- [56] K. Sauer and R. D. Sydora. Current-driven langmuir oscillations and formation of wave packets via modulational instability: Relevance to STEREO observations. *Geophys. Res. Lett.*, 43:7348, 2016.
- [57] S. Humphries. *Charged Particle Beams*. Dover Publications, Inc., New York, 2013.
- [58] S. Ichimaru. *Basic Principles of Plasma Physics: A Statistical Approach*. The Benjamin/Cummings Publishing Company, Inc., Reading, Massachusetts, 1980.
- [59] S. Matsukyo *et al.* Coherent wave forms in the auroral upward current region. *J. Geophys. Res.*, 109:A06212, 2004 doi:10.1029/2004JA010477.
- [60] I. Silin *et al.* Electron beam-plasma interaction: Linear theory and vlasov-poisson simulations. *Phys. Plasmas*, 14:012106, 2007.
- [61] T. Umeda. Vlasov simulation of langmuir wave packets. *Nonlinear Processes Geophys.*, 14:671–67, 2007.
- [62] A. Bruce Langdon Charles K. Birdsall. *Plasma Physics via Computer Simulation*. McGraw-Hill Inc., 1985.
- [63] V. K. Decyk. Description of spectral particle-in-cell codes from the upic framework. *Comp. Phys. Comm.*, 177:95, 2007.
- [64] V. K. Decyk. Description of spectral particle-in-cell codes from the upic framework. <https://picksc.idre.ucla.edu/wp-content/uploads/2015/05/UPICModels.pdf>, Accessed: January 10, 2017.

## BIBLIOGRAPHY

- [65] G. B. Hospodarsky and D. A. Gurnett. Beat-type langmuir wave emissions associated with a type III solar radio burst: Evidence of parametric decay. *Geophys. Res. Lett.*, 22:1161–1164, 1995.
- [66] K. Sigsbee *et al.* Characteristics of langmuir electric field waveforms and power spectra exhibiting nonlinear behavior in earth’s foreshock. *J. Geophys. Res.*, 115:A10251, 2010.
- [67] D. B. Graham and I. H. Cairns. Electrostatic decay of langmuir/z-mode waves in type iii solar radio bursts. *J. Geophys. Res. Space Physics*, 118:3968–3984, 2013.
- [68] R. L. Stenzel. Observation of beam-generated vlf hiss in a large laboratory plasma. *J. Geophys. Res.*, 82:4805–4814, 1977.
- [69] K. Sauer and R. D. Sydora. Mode crossing effects at electron beam-plasma interaction and related phenomena. *Plasma Phys. Control. Fusion*, 54:124045, 2012.
- [70] P. J. Kellog *et al.* Low frequency magnetic signals associated with langmuir waves. *Geophys. Res. Lett.*, 19:1299–1302, 1992.
- [71] O. Moullard *et al.* Whistler waves observed during an in-situ solar type III radio burst. *Astron. Astrophys.*, 335:703–708, 1998.
- [72] V. E. Zakharov. Hamiltonian approach to the dispersion of non-linear phenomena. *Phys. Rep.*, 129:285, 185.

# Appendix

## Dispersion Matrix Formulation

Dispersion of Langmuir/electromagnetic waves in warm electron plasma with warm beam - oblique propagation:

protons (p) are absent,  
main electrons (e) are warm  
beam electrons (b) are warm

The wave (k-vector) propagates in x-direction, the beam (plateau) is inclined to k by the angle  $\Theta$ :

$$V_{bx} = V_b \cos \Theta$$
$$V_{bz} = V_b \sin \Theta$$

System of equations is the following:

$$L E \cdot V_e = c_e E$$

$$L B \cdot V_b = M B \cdot E$$

$$F F E \cdot E = c_j (-D_e V_e - D_b N B \cdot V_b)$$

This gives:

$$V_b = L B^{-1} M B \cdot E$$

$$L E \cdot F F E \cdot E = c_j (-D_e c_e E - D_b (L E \cdot N B) \cdot V_b)$$

$$LE.FFE.E = c_j (-c_e De E - Db (LE.NB).Vb)$$

The dispersion matrix then is given by:

$$MM = LE.FFE + c_j c_e De II + c_j Db (LE.NB).(LBINV.MB)$$

$$c_j = I*y, \quad c_e = I*y,$$

$$\omega = -1$$

$$\omega_b = -1$$

$$c_e = I*y*\omega$$

$$c_j = I*y$$

Definition of the coefficients and matrices:  $x=k$

$$LE = \left\{ \left\{ y^2 - x^2 q_{ve}, 0 \right\}, \right. \\ \left. \left\{ 0, y^2 \right\} \right\}$$

$$LB = \left\{ \left\{ y_b^2 - x^2 q_{vb}, 0 \right\}, \right. \\ \left. \left\{ 0, y_b^2 \right\} \right\}$$

$$y_b = y - x V_b x \\ = y - x V_b \cos t$$

$$WB = \left\{ \left\{ 0, \sin t \right\}, \left\{ 0, -\cos t \right\} \right\} \\ MB = I \omega_b y_b (II - x V_b / y WB)$$

$$KB = \left\{ \left\{ \cos t, \sin t \right\}, \left\{ 0, 0 \right\} \right\} \\ NB = II + (x V_b / y_b) KB$$

$$FF = \left\{ \left\{ y^2, 0 \right\}, \left\{ 0, y^2 - x^2 V^2 \right\} \right\}$$

End of the formulas

Main electron matrix:

$$LE = \left\{ \left\{ LEXX, LEXZ \right\}, \left\{ LEZX, LEZZ \right\} \right\}$$

$$\begin{aligned} \text{LEXX} &= -x^2 qve + y^2 \\ \text{LEXZ} &= 0 \end{aligned}$$

$$\begin{aligned} \text{LEZX} &= 0 \\ \text{LEZZ} &= y^2 \end{aligned}$$

Beam electron matrix:

$$\text{LB} = \{\{\text{LBXX}, \text{LBXZ}\}, \{\text{LBZX}, \text{LBZZ}\}\}$$

$$yb = +(-Vbx*x) + y$$

$$\begin{aligned} \text{LBXX} &= -x^2 qvb + yb^2 \\ \text{LBXZ} &= 0 \end{aligned}$$

$$\begin{aligned} \text{LBZX} &= 0 \\ \text{LBZZ} &= yb^2 \end{aligned}$$

$$\begin{aligned} \text{LBINV} &= \text{Inverse}[\text{LB}] \\ \text{LBINV} &= \text{Simplify}[\text{LBINV}] \end{aligned}$$

$$\begin{aligned} Vbx &= Vb \text{ cost} \\ Vxz &= Vb \text{ sint} \end{aligned}$$

$$\text{II} = \{\{1, 0\}, \{0, 1\}\}$$

$$\begin{aligned} \text{WB} &= \{\{0, \text{sint}\}, \{0, -\text{cost}\}\} \\ \text{MB} &= \text{I omb } yb (\text{II} + (x Vb/y) \text{WB}) \\ \text{MB} &= \text{Simplify}[\text{MB}] \end{aligned}$$

$$\begin{aligned} \text{KB} &= \{\{\text{cost}, 0\}, \{\text{sint}, 0\}\} \\ \text{NB} &= \text{II} + (Vb x/yb) \text{KB} \\ \text{NB} &= \text{Simplify}[\text{NB}] \end{aligned}$$

Maxwell matrix:

$$\begin{aligned} \text{FFXX} &= y^2 \\ \text{FFXZ} &= 0 \end{aligned}$$

```

FFZX= 0
FFZZ= y^2 + (-x^2/VT^2)

FF = {{FFXX,FFXZ},{FFZX,FFZZ}}

```

Constants:

```

ome=-1
omb=-1
ce=I*y*ome
cj=ome*I*y

```

Matrix operations

```

MM = LE.FF + cj ce De II + cj Db (LE.NB).(LBINV.MB)

```

```

MM=Simplify[MM]

```

warm electron plasma

```

qve#0

```

```

warmer Beam

```

```

qvb#0

```

```

DD = Det[MM]

```

```

DD=Expand[DD]

```

```

DD=Together[DD]

```

```

DD=Numerator[DD]

```

```

DD=Factor[DD]

```

```

DD=DD/y^4

```

```

DD=Collect[DD,{y,x,qvb}]

```

```

DD=Together[DD]

```

```

DD=Numerator[DD]

```

```

DD=DD/y^4

```

```

DD=Expand[DD]

```

```

DD=Collect [DD,y]

DDF=FortranForm[DD]

y = k U

DD=Expand[DD]

DD=DD/k^6

DD=Expand[DD]

DD=Collect [DD, {k, U}]

```

Compute the coefficients of the polynomial:

```

DD= C0+C1*Y+C2*Y**2+C3*Y**3+C4*Y**4+C5*Y**5+C6*Y**6

X: norm. wavenumber

REAL COEF (7)

REAL Nbeam

      GAMMAE=3.          ! GAMMA=3/2
QVE=GAMMAE
QVC=QVE
      QVB=QVC*VTbeam**2      ! VTbeam: Ratio between therm. Speed.

VT=VTc          ! Therm. Speed./c

Db = Nbeam
Vb = Vbeam

DE=1.0 - Db

V0 = Vb

```

ALFA=Db

$$\text{cost}=\cos(3.1414*\text{Teta}/180.)$$

Coefficients of the polynomial:

Coefficients of the six prder polynomial:

$$\begin{aligned} \text{C0} = & (-\text{Db}*\text{De}*\text{qvb}*\text{VT}^2) - \text{De}^2*\text{qvb}*\text{VT}^2 - \text{Db}^2*\text{qve}*\text{VT}^2 \\ & 1 - \text{Db}*\text{De}*\text{qve}*\text{VT}^2 + \text{cost}^2*\text{Db}*\text{De}*\text{Vb}^2*\text{VT}^2 \\ & 1 + \text{cost}^2*\text{De}^2*\text{Vb}^2*\text{VT}^2 + \text{Db}*\text{De}*\text{shint}^2*\text{Vb}^2*\text{VT}^2) *x^2 \\ & 1 + (-\text{De}*\text{qvb}) - \text{Db}*\text{qve} + \text{cost}^2*\text{De}*\text{Vb}^2 - \text{Db}*\text{qvb}*\text{qve}*\text{VT}^2 \\ & 1 - \text{De}*\text{qvb}*\text{qve}*\text{VT}^2 + \text{cost}^2*\text{Db}*\text{qve}*\text{Vb}^2*\text{VT}^2 \\ & 1 + \text{cost}^2*\text{De}*\text{qve}*\text{Vb}^2*\text{VT}^2 \\ & 1 + \text{Db}*\text{qve}*\text{shint}^2*\text{Vb}^2*\text{VT}^2) *x^4 \\ & 1 + (-\text{qvb}*\text{qve}) + \text{cost}^2*\text{qve}*\text{Vb}^2) *x^6 \end{aligned}$$

$$\begin{aligned} \text{C1} = & + ((-2*\text{cost}*\text{Db}*\text{De}*\text{Vb}*\text{VT}^2 - 2*\text{cost}*\text{De}^2*\text{Vb}*\text{VT}^2) *x \\ & 1 + (-2*\text{cost}*\text{De}*\text{Vb} - 2*\text{cost}*\text{Db}*\text{qve}*\text{Vb}*\text{VT}^2 \\ & 1 - 2*\text{cost}*\text{De}*\text{qve}*\text{Vb}*\text{VT}^2) *x^3 - 2*\text{cost}*\text{qve}*\text{Vb} *x^5) \end{aligned}$$

$$\begin{aligned} \text{C2} = & + (\text{Db}^2*\text{VT}^2 + 2*\text{Db}*\text{De}*\text{VT}^2 + \text{De}^2*\text{VT}^2 \\ & 1 + (\text{Db} + \text{De} + \text{Db}*\text{qvb}*\text{VT}^2 + 2*\text{De}*\text{qvb}*\text{VT}^2 + 2*\text{Db}*\text{qve}*\text{VT}^2 \\ & 1 + \text{De}*\text{qve}*\text{VT}^2 - \text{cost}^2*\text{Db}*\text{Vb}^2*\text{VT}^2 \\ & 1 - 2*\text{cost}^2*\text{De}*\text{Vb}^2*\text{VT}^2 - \text{Db}*\text{shint}^2*\text{Vb}^2*\text{VT}^2) *x^2 \\ & 1 + (\text{qvb} + \text{qve} - \text{cost}^2*\text{Vb}^2 + \text{qvb}*\text{qve}*\text{VT}^2 \\ & 1 - \text{cost}^2*\text{qve}*\text{Vb}^2*\text{VT}^2) *x^4) \end{aligned}$$

$$\begin{aligned} \text{C3} = & + ((2*\text{cost}*\text{Db}*\text{Vb}*\text{VT}^2 + 4*\text{cost}*\text{De}*\text{Vb}*\text{VT}^2) *x \\ & 1 + (2*\text{cost}*\text{Vb} + 2*\text{cost}*\text{qve}*\text{Vb}*\text{VT}^2) *x^3) \end{aligned}$$

$$\begin{aligned} \text{C4} = & + (-2*\text{Db}*\text{VT}^2 - 2*\text{De}*\text{VT}^2 + (-1 - \text{qvb}*\text{VT}^2 - \text{qve}*\text{VT}^2 \\ & 1 + \text{cost}^2*\text{Vb}^2*\text{VT}^2) *x^2) \end{aligned}$$

$$\text{C5} = - 2*\text{cost}*\text{Vb}*\text{VT}^2*x$$

$$\text{C6} = + \text{VT}^2$$